



Review

# A Review on Lithium-Ion Battery Modeling from Mechanism-Based and Data-Driven Perspectives

Cheng Ji <sup>1</sup>, Jindong Dai <sup>1</sup>, Chi Zhai <sup>2</sup> , Jingde Wang <sup>1</sup>, Yuhe Tian <sup>3,\*</sup> and Wei Sun <sup>1,\*</sup> 

<sup>1</sup> College of Chemical Engineering, Beijing University of Chemical Technology, 15 North Third Ring Road, Chaoyang District, Beijing 100029, China; 202470006@mail.buct.edu.cn (C.J.); 2021400012@buct.edu.cn (J.D.); jingdewang@buct.edu.cn (J.W.)

<sup>2</sup> Faculty of Chemical Engineering, Kunming University of Science and Technology, Kunming 650500, China; zhaichi@kmust.edu.cn

<sup>3</sup> Chemical and Biomedical Department, West Virginia University, Morgantown, WV 26506, USA

\* Correspondence: yuhe.tian@mail.wvu.edu (Y.T.); sunwei@mail.buct.edu.cn (W.S.)

**Abstract:** As the low-carbon economy continues to advance, New Energy Vehicles (NEVs) have risen to prominence in the automotive industry. The design and utilization of lithium-ion batteries (LIBs), which are core component of NEVs, are directly related to the safety and range performance of electric vehicles. The requirements for a refined design of lithium-ion battery electrode structures and the intelligent adjustment of charging modes have attracted extensive research from both academia and industry. LIB models can be divided into mechanism-based models and data-driven models; however, the distinctions and connections between these two kinds of models have not been systematically reviewed as yet. Therefore, this work provides an overview and perspectives on LIB modeling from both mechanism-based and data-driven perspectives. Meanwhile, the potential fusion modeling frameworks including mechanism information and a data-driven method are also summarized. An introduction to LIB modeling technologies is presented, along with the current challenges and opportunities. From the mechanism-based perspective of LIB structure design, we further explore how electrode morphology and aging-related side reactions impact battery performance. Furthermore, within the realm of battery operation, the utilization of data-driven models that leverage machine learning techniques to estimate battery health status is investigated. The bottlenecks for the design, state estimation, and operational optimization of LIBs and potential prospects for mechanism-data hybrid modeling are highlighted at the end. This work is expected to assist researchers and engineers in uncovering the potential value of mechanism information and operation data, thereby facilitating the intelligent transformation of the lithium-ion battery industry towards energy conservation and efficiency enhancement.

**Keywords:** lithium-ion batteries; mechanism modeling; data-driven modeling; battery aging mechanism; structure–activity relationship; state of health estimation



**Citation:** Ji, C.; Dai, J.; Zhai, C.; Wang, J.; Tian, Y.; Sun, W. A Review on Lithium-Ion Battery Modeling from Mechanism-Based and Data-Driven Perspectives. *Processes* **2024**, *12*, 1871. <https://doi.org/10.3390/pr12091871>

Academic Editors: Elio Santacesaria, Riccardo Tesser and Vincenzo Russo

Received: 1 August 2024

Revised: 24 August 2024

Accepted: 28 August 2024

Published: 1 September 2024



**Copyright:** © 2024 by the authors. Licensee MDPI, Basel, Switzerland. This article is an open access article distributed under the terms and conditions of the Creative Commons Attribution (CC BY) license (<https://creativecommons.org/licenses/by/4.0/>).

## 1. Introduction

Lithium-ion batteries (LIBs) are environment-friendly energy storage tools that exhibit numerous advantages. Their remarkable energy density, coupled with extensive recyclability and a minimal self-discharge rate, positions them as highly promising candidates for wide applications in the field of energy storage [1,2]. Currently, the application of LIBs is experiencing a crucial stage of rapid expansion across diverse scenarios such as electric vehicles, portable electronic devices, and energy storage systems [3,4]. They serve as a key technology in energy transition, thereby facilitating the optimization and upgrading of the energy structure [5]. At the current stage, the development and application of LIBs still face obstacles, notably the further enhancement of charging speed and the significant decline in battery capacity after multiple charge–discharge cycles [6]. These limitations have ignited widespread research interest among both academia and industry [7–10].

At the stage of battery design, it is imperative to conduct a comprehensive exploration of the internal micro-operation mechanism within the battery, which could underly the influence of internal and external factors on battery performance, ultimately facilitating the design of optimal electrode structures that exhibit significantly enhanced overall performance. Regarding the operational level of batteries, it is necessary to accurately estimate the operating status, State of Health (SOH), and the remaining capacity of the battery throughout the charge–discharge cycle. This information is essential not only for ensuring the safety of the battery system but also for guiding the development of optimized charging and discharging strategies that maximize battery performance and lifespan [11]. Generally, mechanism models that rely on mathematical equations offer invaluable assistance to researchers in exploring the structure–activity relationship within batteries, thereby reducing experimental costs and enhancing research efficiency, while data-driven models that leverage data collected during the battery cycling process can easily and efficiently predict changes in both the State of Charge and health of the battery to improve the intelligence level of the battery management system (BMS) [12–15]. Existing review articles mostly tend to concentrate either exclusively on data-driven modeling approaches or solely on mechanism-based modeling frameworks. To set our work apart from the existing literature, the existing battery models from the perspectives of a data-driven and intrinsic mechanism are both reviewed in this paper; on this basis, the exploration of data–mechanism hybrid modeling is also summarized, considered as a potential research direction to overcome the limitations in single data-driven models and single mechanism models.

For mechanism models, various complex electrochemical and physical processes occur inside LIBs, e.g., the transportation of ions through the electrolyte, their insertion and extraction at the electrode surfaces, and their diffusion within the electrode materials, etc. Additionally, the performance of the LIBs is also influenced by multiple factors, such as the choice of electrode materials and electrolyte types, the manufacturing processes adopted to prepare the electrodes, and the operating conditions during repeated cycling. Studying the influence of various factors on different processes in batteries to improve their performance has always been an important issue of concern [16]. However, LIBs exhibit spatial multi-scale characteristics ranging from electrode particles to the overall battery, as well as temporal cross-scale characteristics spanning microscopic ion movements to thousands of cycles of battery aging in practical applications. This complexity has led to a fragmentation of research concerns, and simultaneously poses challenges in correlating research findings at smaller scales with practical applications at higher scales. On the other hand, the physical and chemical changes occurring inside the battery during its operation can be reflected in the process data collected by the sensors, including variables such as current, voltage, internal resistance, impedance, and maximum available capacity, which in turn can indirectly indicate the SOH of LIBs. With sufficient historical data, data-driven models can feasibly fit the changes in the internal and external characteristic parameters of the battery over time, enabling the precise acquisition of the real-time health status of LIBs. In particular, the development of machine learning (ML) technology has led to the development and application of numerous advanced artificial intelligence (AI) algorithms in LIB modeling. These algorithms have achieved remarkable results in terms of accuracy while simultaneously demonstrating superior computational efficiency, which is difficult to match by a mechanistic model [17]. Despite their numerous advantages, data-driven models predominantly operate as black boxes, whose generalization capabilities are limited by the quality and comprehensiveness of historical data. Furthermore, the features extracted from these models often lack interpretability, which hinders their practical application in performance prediction and optimization for batteries over long usage cycles [18].

Overall, the primary objective of this paper is to comprehensively review existing mechanistic models and data-driven models, with a particular emphasis on the application of ML in the data-driven modeling for LIBs. The strengths, limitations, and scopes of applicability of the different methods are discussed, offering researchers valuable insights for model selection in their studies. Meanwhile, the opportunities and challenges faced

by the development of LIB models are summarized, through which future advancements in the field of LIB modeling are expected to be clearly outlined. Through this study, it is expected to systematically sort through the advancement of the modeling technology of LIBs to reveal potential research directions and clarify the differences and connections between the data-driven models and mechanism models, so as to provide a reference for researchers in model selection.

The remainder of this paper is organized as follows: A comprehensive review of mechanism models for LIBs is presented in Section 2. In Section 3, the data-driven LIB modeling methods are summarized, and a generic data-driven framework is introduced. Challenges and future research prospects for LIB modeling are discussed in Section 4. Then, this paper is concluded in Section 5.

## 2. A Comprehensive Review of Mechanism Models for LIBs

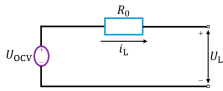
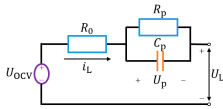
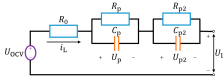
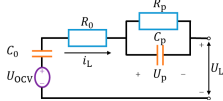
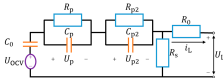
Mechanism models typically rely on a preset battery physical model (such as equivalent circuit models [19,20], electrochemical models [21], thermodynamic models [22], and diffusion models [23], etc.) to obtain characteristic parameters that can represent the physical and chemical changes occurring inside the battery, by which the impacts of material properties and electrode structure on battery performance can be further analyzed, making them an effective tool to assist in the design of electrode structures. This section presents an overview of several prevalent mechanistic models employed for LIB modeling. The incorporation of electrode morphology and battery aging processes in the long-cycle modeling of LIBs and their impact on the battery performance considered in these models are investigated.

### 2.1. Mechanism Models for LIBs

#### 2.1.1. Equivalent Circuit Model

The equivalent circuit model serves as a crucial tool in circuit analysis and design. By constructing circuits with a range of electronic components such as resistors, capacitors, and power sources, it provides a means to describe the dynamic characteristics of batteries. However, it does not take into account the physicochemical processes occurring within the battery [24]. Table 1 presents five common equivalent circuit models: the Rint model [25], the Thevenin model [26], the second-order RC model [27,28], the PNGV model [29,30], and the GNL model [31].

**Table 1.** A brief overview of common equivalent circuit models.

Types	Schematic	State Equation
The Rint model		$U_L(t) = U_{OCV}(t) - i_L(t)R_0$
The Thevenin model		$U_L(t) = U_{OCV}(t) - U_p(t) - i_L(t)R_0$
The second-order RC model		$U_L(t) = U_{OCV}(t) - U_p(t) - U_{p2}(t) - i_L(t)R_0$
The PNGV model		$U_L(t) = U_{OCV}(t) - U_0(t) - U_p(t) - i_L(t)R_0$
The GNL model		$U_L(t) = U_{OCV}(t) - U_0(t) - U_p(t) - U_{p2}(t) - i_L(t)R_0$

In general, the more complex the structure of the equivalent circuit model, the higher the estimation accuracy of the battery's electrochemical information, accompanied by a greater computational load. Therefore, when selecting a model in practice, it is necessary to choose an appropriate equivalent circuit model based on the battery type and research objectives. Meanwhile, the resistance and capacitance in the equivalent circuit model are time-varying because of the impact of the charging rate, temperature, etc. Parameter identification is necessary in the equivalent circuit model to adapt to practical operations [32]. Although the equivalent circuit model is more convenient to calculate than the traditional electrochemical model, it does not consider the physical and chemical reactions inside the battery, making it insufficient for analyzing various influencing factors within the battery.

### 2.1.2. Pseudo-Two-Dimensional (P2D) Model

The electrochemical model delves deeply into the microscopic reaction characteristics of batteries, including electrochemical reactions such as liquid-phase diffusion, solid-phase diffusion, and migration. The initial electrochemical model was based on porous electrode and concentrated solution theories, which utilized a series of Partial Differential Equations (PDEs) and algebraic equations related to battery ion concentration and electric potential to describe the operating state of batteries [33,34]. Currently, most electrochemical models of LIBs are developed from the classical P2D model, which relies on porous electrode theory and the Butler-Volmer (BV) interfacial reaction equation to calculate physicochemical processes across three scales: particle, electrode, and battery [35–37]. In 1975, Newman and Tiedemann first introduced the porous electrode theory [38], which divides the interior of a battery into two regions: solid phase and liquid phase. The solid phase consists of solid particles, while the liquid phase comprises the electrolyte within the pores. Furthermore, they subdivided the charging and discharging processes of lithium-ion batteries into four crucial steps: solid-phase diffusion, liquid-phase diffusion, electromigration, and electrochemical reactions.

Upon the robust foundation of the porous electrode theory, Doyle et al. further constructed the P2D battery model, which is shown in Figure 1 [39]. The characteristic of this P2D model lies in its simplification of the lithium-ion diffusion process within the solid-phase particles. Specifically, the process is simplified by considering only the diffusion along the radial direction ( $R$ ) of spherical particles, thereby achieving dimensionality reduction in the model. Meanwhile, owing to the minute size of the spherical particles in comparison to the liquid phase, the model assumes that the solid-phase concentration at each point in the liquid phase is determined by the diffusion equation along the  $R$  direction, and the electrode particles are presumed to be of uniform size and evenly distributed. On the other hand, the lithium ions in the liquid phase undergo diffusion and electromigration along the  $x$  direction. Due to the continuity assumption, each point along the  $x$  direction possesses a corresponding solid-phase condition, implying the continuous presence of both solid and liquid phases along the  $x$  axis. The material exchange between the solid and liquid phases at each point is computationally determined by the BV equation.

The mathematical equations included in the P2D model are comprised of six parts [39]:

- (1) The concentration distribution equation of lithium ions in the solid phase (along the  $r$  direction).

$$\frac{\partial c_s}{\partial t} = \frac{D_s}{r^2} \frac{\partial}{\partial r} \left( r^2 \frac{\partial c_s}{\partial r} \right) \quad (1)$$

where  $c_s$  denotes the solid-phase lithium-ion concentration,  $D_s$  represents the solid-phase diffusion coefficient,  $r$  is the distance from the center of a spherical particle, and  $t$  stands for time. During the charge and discharge of the battery, lithium ions at the positive and negative electrodes gradually diffuse out of the crystal lattice of the electrode material. Lithium ions mainly move through diffusion in the solid-phase particles inside the battery.

- (2) The concentration distribution equation of lithium ions in the liquid phase (along the  $x$  direction).

$$\varepsilon_e \frac{\partial c_e}{\partial t} = D_e \frac{\partial^2 c_e}{\partial x^2} + \frac{1 - t_+^0}{F} J^{Li} \quad (2)$$

where  $c_e$  denotes the concentration of the liquid phase,  $D_e$  represents the diffusion coefficient of the liquid phase,  $t_+^0$  is the transference number,  $J^{Li}$  stands for the solid–liquid interfacial flux of lithium ions, and  $F$  is the Faraday constant. During the charging and discharging process of a battery, lithium ions diffuse in the electrolyte due to concentration gradients and undergo electromigration under the influence of an electric field, enabling continuous transport between the anode and cathode. Consequently, the temporal distribution of lithium-ion concentration within the electrolyte can be described as Equation (2).

- (3) The electric potential distribution in the solid phase.

$$\sigma \frac{\partial^2 \phi_s}{\partial x^2} = J^{Li} \quad (3)$$

where  $\phi_s$  denotes the electric potential in the solid phase and  $\sigma$  represents the electrical conductivity in the solid phase. The variation in electric potential distribution within solid particles can be represented using Ohm's law for porous electrodes, as shown in Equation (3).

- (4) The electric potential distribution in the liquid phase

$$\kappa^{eff} \frac{\partial^2 \phi_e}{\partial x^2} + \frac{\kappa_d^{dff}}{c_{e,0}} \frac{\partial^2 c_e}{\partial x^2} + J^{Li} = 0 \quad (4)$$

$$\kappa_d^{eff} = \frac{2RT\kappa^{eff}}{F} (t_+^0 - 1) \left( 1 + \frac{d \ln f}{d \ln c_e} \right) \quad (5)$$

The electric potential distribution in the liquid phase is described using a modified Ohm's law for porous electrodes, as shown in Equations (4) and (5), where  $\phi_e$  denotes the liquid-phase electric potential,  $\kappa^{eff}$  represents the effective liquid-phase conductivity,  $\kappa_d^{eff}$  is the effective diffusion conductivity, and  $f$  stands for the ionic activity coefficient.

- (5) The BV equation.

$$J^{Li} = kc_e^{0.5} (c_{s,max} - c_{s,surf})^{0.5} c_{s,surf}^{0.5} \left( \exp\left(\frac{\alpha F \eta}{RT}\right) - \exp\left(\frac{-\alpha F \eta}{RT}\right) \right) \quad (6)$$

$$\eta = \phi_s - \phi_e - E_0 \quad (7)$$

where  $c_{s,max}$  denotes the maximum particle concentration,  $c_{s,surf}$  represents the particle surface concentration,  $\alpha$  is the electrode transfer coefficient,  $\eta_r$  stands for the reaction overpotential, and  $E_0$  is the equilibrium potential related to the properties of the electrode and particles. The BV equation can be employed to describe the relationship between the overpotential at the surface of a positive solid spherical particle and the flux of lithium ions through the surface of the particle.

- (6) The terminal voltage of the battery.

$$V(t) = \phi_s(L, t) - \phi_s(0, t) \quad (8)$$

The difference between the solid-phase potential at the rightmost side of the battery and the solid-phase potential at the leftmost side represents the terminal voltage of the battery. The terminal voltage is a crucial variable that indicates the load conditions of the battery and is frequently used for validation between the P2D model and experimental data.

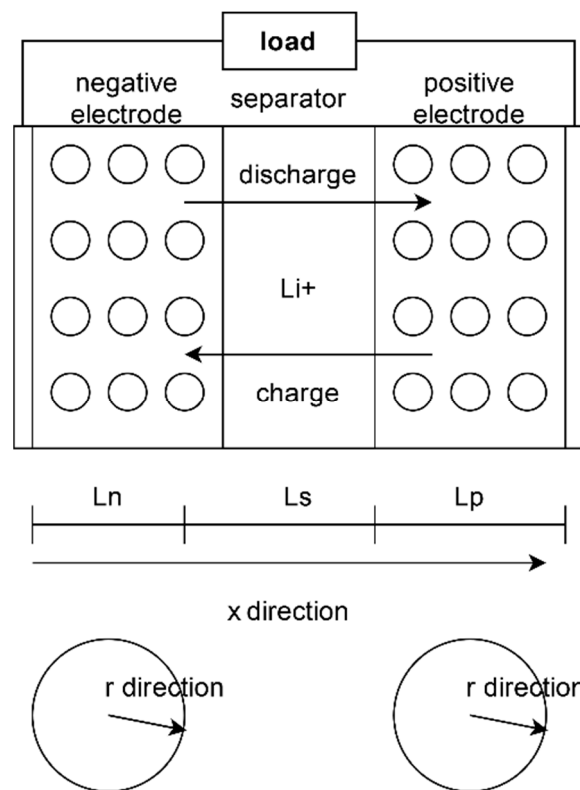


**Figure 1.** The schematic diagram of the P2D model for LIBs.

Moreover, the boundary conditions of the model vary according to different charging and discharging conditions. For instance, during constant current charging, the partial derivative of the potential at the cathode current collector in the  $x$  direction is set to the specified current value. In contrast, during constant voltage charging, the potential difference between the two boundaries is maintained as constant. Detailed boundary conditions can be found in the reference of Mu et al. [40].

Depending on diverse research objectives, the P2D model can be further simplified or complicated accordingly. Its development trends can be mainly categorized into three directions. The first one is to progress towards a microscopic scale, enhancing the characterization of the mass transfer process within solid particles to investigate how particle morphology influences battery performance. Another direction is to integrate it with multi-physics fields to involve the impact of environmental variables such as temperature. The last one is to simplify the model to accelerate its solution process, to meet the demands of the online management of battery systems and optimal battery design.

For the first direction, it is difficult to study the impact of irregular particle shapes and an uneven particle distribution on battery performance using the P2D model because it assumes that spherical particles are uniformly dispersed. However, it has been verified through experiments that the non-uniformity of particles is a potential factor in improving the battery performance mentioned above. To overcome this limitation, Jiang et al. established a realistic two-dimensional model of LIBs, in which every part of the P2D model was extended into two dimensions and a quadruple-structure generation algorithm was utilized to create solid-phase particles with irregular shapes and discontinuous distributions [41]. This approach was used to study the relationship between electrode microstructure and battery performance, and it reached the conclusion that large negative electrode particles with low porosity and small positive electrode particles with high porosity can effectively enhance battery performance. Inspired by this work, Kespe and Nirschl further established a three-dimensional model based on the P2D model theory, and approximated the morphology and distribution of electrode particles with spherical particles of different sizes to

make the model close to reality [42]. It was concluded through simulation that arranging small particles near the separator can help delay the degradation process of the electrolyte in high-power applications. Furthermore, Lu et al. considered complex physicochemical processes across multiple length scales in their three-dimensional battery model, enabling the collaborative study of the influence of crystal orientation at the single-particle level and particle distribution at the electrode level [43]. However, the above simulation methods are all based on PDEs, which require a large number of iterative solutions when faced with irregular solid–liquid boundary conditions, leading to slow computation speeds and high computational costs, making them impractical for fine-scale simulation and emulation.

For the second aspect, the interaction of multiple physical fields is ever-present in complex electrochemical systems like LIBs. Beyond the fundamental concentration and electric fields, the impact of the temperature field cannot be ignored. An excessively high temperature could trigger battery side reactions, significantly increase thermal stress, shorten battery lifespan, and even lead to safety accidents. Conversely, an excessively low temperature will pose difficulties for the charging and discharging process of LIBs, hindering the full expression of their performance. Since the traditional P2D model is based on the assumption of isothermal conditions, incorporating thermal effects into the model has emerged as a significant area of battery research, which could contribute to battery safety design and the optimization of charging and discharging strategies. Li et al. integrated the P2D model with a thermal model to establish an electrochemical–thermal coupling model, which is capable of solving the temperature distribution within batteries [44]. Building upon this foundation, researchers have incorporated various heat transfer mechanisms into the electrochemical–thermal coupling model to investigate battery heat dissipation, expanding from understanding the heat generation patterns of individual cells to designing external cooling strategies for battery systems, including external air cooling, liquid cooling, and phase-change material cooling, etc. [45]. In the design of battery thermal management systems, researchers have discovered that temperature is also related to abnormal battery expansion, which can lead to electrolyte leakage, battery short circuits, and other failures. Consequently, the factor of the stress field has been introduced into the model design, accounting for stress variations induced by temperature and pressure changes [46]. Overall, battery simulation and modeling have evolved into a multi-physics coupling framework encompassing electric, thermal, and stress fields. As an open-ended model, the P2D model serves as a foundational platform that can interface and couple with various physical fields.

For the last research scope, effective numerical methods or model reduction approaches are adopted to reduce the computational complexity of PDE models. Among the reduced-order models, the simplest form is the Single Particle Model (SPM) [47], where both the cathode and anode are represented by a single spherical particle, while the influence of the electrolyte is neglected. Although the computational loads of the model can be significantly reduced, its accuracy can deteriorate rapidly when high current densities are applied due to the apparent diffusion limitations within the electrolyte [48]. To expand the application scope of the SPM, the diffusion of lithium ions in the electrolyte phase [49] and thermal behavior in electrodes [50] have been introduced, while the heterogeneity of particles remains unconsidered within the SPM framework. To address this gap, the Multi-Particle Model (MPM) was proposed to extend the SPM by incorporating electrode particles with varying radii and contact resistances [51]. When the charge–discharge rate exceeds 1C, the voltage curve accuracy of the MPM is notably higher than that of the SPM, but the increase in the number of parameters also imposes a heavier burden on the parameter identification [52]. Another dimension reduction approach is the multi-scale, multi-domain (MSMD) model [53], which divides the spatial domain into particle, electrode, and battery domains based on different length scales, with only average values shared between adjacent domains. The MSMD model considers the states of various internal components of the battery while maintaining high computational efficiency. However, its spatial resolution is limited, as only averages are exchanged between domains.

Allu et al. [54] employed a set of mesoscopic volume elements to describe mass and charge transport within electrodes, in which governing equations were solved within each representative volume element and then the volume-averaging approach was applied to obtain macroscopic variable values. This model could consider three-dimensional information while effectively reducing computational costs through volume averaging, which represents a promising dimension reduction method. Nevertheless, electrode particles are still assumed to be spherical, and the diffusion equations in the solid phase need to be solved for each volume element. Hence, irregular electrode morphologies are not considered in this model, and it is better for the number of diffusion equations to be reduced. Additionally, there are also numerous numerical schemes to mitigate the computational burden of PDE models. The finite difference (FD) [55] and finite element (FE) [56] methods are two of the most commonly used approaches, in which PDEs are only discretized in the spatial or spatio-temporal domain to transform them into Differential Algebraic Equations (DAEs) or algebraic equations (AEs) [57]. An alternative efficient numerical technique is the Orthogonal Collocation Method (OCM) [58,59], where the PDE solution is assumed as a sum of orthogonal polynomials. After appropriate coordinate transformations, the collocation method is used to determine the polynomial coefficients. Nonetheless, the number of discrete algebraic equations depends on the initial PDE model, and the solution of nonlinear algebraic equations remains challenging, which indicates that combining model reduction methods with numerical techniques is a more promising direction than only relying on a single approach.

### 2.1.3. Cellular Automata (CA) Model

As mentioned before, LIB models are primarily described by PDEs. CA, as a discrete modeling framework, can also be employed to depict the evolution of system states over time and space [60]. The differential equation model is established based on the conservation laws and differential units within the system, to derive the distribution functions of variables in continuous time and space. In contrast, the CA model is established based on flexible interaction rules among cells, which are not constrained by closed or continuous assumptions but place greater emphasis on local mechanisms. It is worth noting that CA and differential equation methods are not mutually exclusive. They can be combined or alternated, since differential equations often require discretization in their solution process. In 1986, Wolfram suggested that CA can be adopted to approximate any differential equation system by introducing finite differences or finite elements [61]. When cells are assumed to be differentiable units, they can be equivalent to different equations describing continuous regions. Although the CA model inherently suffers from the limitation of unclear physical meaning, its excellent compatibility with other methods can effectively compensate for this limitation. A promising direction for the development of CA models is to combine CA with other algorithms into a framework, where each method leverages its unique strengths.

Similar to the P2D model, the CA model has also evolved into various forms to adapt to different research demands. The CA model was first introduced by John von Neumann in 1966 and gained significant attention from researchers in 1970 due to the self-organizing behavior from disorder to order demonstrated by the “Game of Life”. In 1986, Stephen Wolfram systematically classified various rules and phenomena of CA, leading to the emergence of variants such as Lattice Gas Automata [62], Margolus CA [63], Lattice Boltzmann CA [64], and Diffusion-Limited Aggregation (DLA) CA [65] to correspond to different physicochemical processes. These forms all adhere to the principle of simulating and evolving complex system behaviors through the interaction of local units.

The diffusion process represented the initial application of CA to practical physical processes. Both the Lattice Gas Automata [66] and the naive CA diffusion models [67] achieve the simulation of concentration diffusion in gases and liquids through the random exchanges between cells and their neighbors, which is essentially derived from the concept of Brownian motion, i.e., the perpetual and irregular motion of particles suspended in gases



or liquids. However, in this model, cells can only be updated asynchronously, because synchronous updates would lead to the disappearance or increase of particles, which violates the law of conservation of mass. Bandman introduced convection processes into Margolus CA by incorporating unequal clockwise and counterclockwise rotation probabilities and simulated the fluid flow in irregularly shaped media [68]. Ai et al. discussed the grid anisotropy of propagation fronts in CA and applied it to simulate crystallization processes [69]. Gurikov used the Margolus scheme to study diffusion and adsorption phenomena in porous media [70], but the physical quantities were dimensionless, and the relationship between CA diffusion results and actual diffusion coefficients remains unclear, requiring further research.

As for the chemical reactions, Ai et al. simulated the spatio-temporal evolution of the Belousov–Zhabotinsky (BZ) reaction using CA [71], and validated their results against traditional finite difference methods. The establishment of this rule captured the essence of the mutual conversion between the three reactants in the BZ reaction. Different substances are represented by discrete cells, and their mutual conversion rules are set, thereby simulating spatial oscillation phenomena such as chemical waves. Ackland and Tweedie [72] proposed a Lattice Boltzmann CA model based on DLA theory to simulate dendrite growth processes in lithium metal electrodes. The basic rule is that ion cells randomly walk in the liquid-phase space, and their reaction probability is calculated based on conditions such as current density and concentration when they approach crystal cells, thereby becoming new crystal cells. Applying such simple rules globally can achieve the simulation of complex dendrite morphology growth processes, which demonstrates the advantages of CA.

Brokate et al. [73] utilized CA to simulate redox reactions on the surface of flat electrodes, where the reaction probability of discrete ion cells upon contacting electrode cells was calculated based on the Nernst equation. The simulation results were consistent with those calculated using differential equations, while also providing the visualization of spatial dynamic results. The Lattice Boltzmann CA has a closer relationship with differential equations and can be seen as a numerical solution method for PDEs. By statistically analyzing information on the velocity, temperature, and other aspects of a large number of discrete particles, macroscopic characteristics of fluid motion can be obtained. The consistency of its calculation results with finite difference methods proves the dialectical unity between fluid continuity and discreteness. Jiang et al. [41] used the Lattice Boltzmann method to solve the classical P2D model, demonstrating a significantly increased computational speed compared to finite difference methods while maintaining a similar accuracy. Du et al. constructed a CA-LBM framework that combined the strengths of CA and Lattice Boltzmann Method (LBM) to simulate the lithium dendrite growth process [74].

However, existing CA models have not yet considered the influence of porous structures on reaction–diffusion processes. Given the advantages of CA, such as the ease of setting complex boundaries, its suitability for parallel computing, and simplicity in program implementation, it is worthwhile to integrate particle-scale models with battery-scale models using CA to further investigate the impact of porous structural information on battery performance.

## 2.2. The Incorporation of Electrode Morphology in Mechanism Models

The microstructure of electrodes plays a crucial role in the electrochemical performance of LIBs. The porosity and particle-size distribution of electrodes are the most commonly used parameters in electrode structure design [75]. During the charging process, the speed of electron transfer is faster than that of ion diffusion, leading to the accumulation of electrons on the surface of electrode particles. This accumulation forms an additional potential difference, which acts as a driving force to facilitate ion migration. The voltage curve during the constant current charging of a battery, as shown in Figure 2, indicates that the constant current represents a consistent total amount of electrons entering the electrode per unit time. The local overpotential resulting from electron accumulation serves as the impetus

for the reaction to occur. The equilibrium voltage displayed in the figure corresponds to the required driving force for the lithium-ion intercalation reaction. However, a reaction cannot occur when the overpotential is exactly equal to the equilibrium potential, as the battery requires additional overpotential to enable ions to pass through the membrane on the particle surface. This additional potential is termed the ohmic polarization voltage [76]. Additionally, another portion of extra potential, known as the concentration polarization voltage, is necessary to promote the concentration diffusion of ions. Polarization refers to the deviation of the electrode potential from its equilibrium state [77]. Higher polarization voltages lead to a lower actual charge capacity when the battery is charged to the cut-off voltage, resulting in lower charging efficiency. Therefore, a method to enhance battery-charging efficiency is to improve the mass transfer capability within electrode particles and the electrolyte phase, which is closely related to the microstructure of electrode particles [78]. On the other hand, the energy density performance of a battery is determined by the solid-phase fraction of electrode particles. Generally, a lower electrode porosity and higher electrode thickness lead to the higher storage capacity of the battery [79].

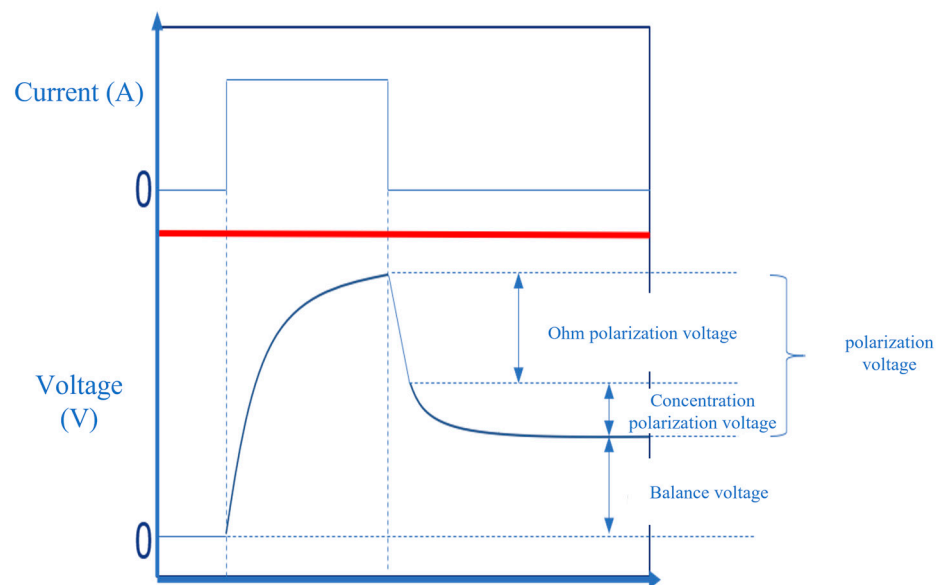


**Figure 2.** Diagram of polarization voltage of each part.

Chen et al. [80] indicated that the selection of porosity during electrode manufacturing requires a trade-off between electronic conductivity and ion transport. While a higher porosity facilitates iron transport, it also reduces electronic conductivity and energy density. Zheng et al. [81] proposed a correlation between electrode inactive components and the optimal porosity, with an optimal porosity of 30% and an inactive component mass fraction of 8%. Zaghbi discovered that a gradient distribution of lithium ions occurs in electrode particles with larger radii, implying that the solid-phase transport rate is the primary limiting factor during charging [82]. Lu and Lin [83] found that when lithium manganate is used as the cathode material, smaller electrode particles provide a larger reaction surface area, corresponding to a higher charge–discharge efficiency. Sivakkumar et al. [84] showed through experimental data that an increase in the average particle size leads to the improved initial charge–discharge efficiency of the battery, which corresponds to the formation of a thinner Solid Electrolyte Interface (SEI) and higher battery capacity. With advancements in electrode-manufacturing technology, the shape and orientation of electrode particles can be controlled more precisely. Frankenberger et al. [85] utilized a magnetic field during the coating process to control the orientation of graphite particles perpendicular to the collector surface, which could effectively reduce liquid-phase transport resistance and enhance charging efficiency. Furthermore, a set of electrodes composed of parallel graphite

sheets was prepared using a magnetic field, whose rate capability was three times higher than that of traditional electrode structures.

While these insightful findings are based on experiments, exploring a range of electrodes with different microstructures through experimentation is costly and time-consuming. During multi-step preparation processes, uncertainties make it challenging to control particle morphology. Therefore, numerous studies on electrode structure optimization have been conducted in collaboration with numerical simulation methods. Kalnaus et al. [86] designed a two-layer electrode consisting of a “power layer” and an “energy layer”, utilizing different porosities in each layer to achieve a higher discharge capacity. Methekar et al. [87] designed a gradient porosity electrode and optimized the porosity distribution across the electrode thickness to minimize electrode resistance. Qi et al. [88] also designed a two-layer electrode and achieved multi-objective optimization by adjusting the porosity of each layer to reduce both resistance and overpotential. More complex layering schemes and optimization functions have also been investigated in the literature [89,90]. It is concluded that increasing porosity towards the separator is beneficial for both power and capacity.

Apart from porosity distribution, electrode performance is also influenced by particle-size distribution. Bläubaum et al. [91] reported that a smaller mean particle size with lower variance leads to a better performance in high-current applications. Taleghani et al. [92] studied the effects of different particle-size distributions using an extended P2D model. The results showed that the concentration polarization effect is lower for unimodal distributions compared to bimodal and trimodal distributions. Kanchan and Randive [93] designed a gradient particle-size electrode structure and demonstrated its superiority in reducing capacity fade rates through simulation. More studies on the impact of electrode structures on battery performance can be found in review papers [94,95].

However, existing battery models struggle to balance high computational efficiency with a detailed consideration of electrode morphology, which is crucial in electrode structure design. There is a need to develop a more advanced electrochemical model that captures the internal state of the battery, including a detailed electrode morphology, while maintaining sufficient computational efficiency to meet the requirements of electrode morphology optimization and long-term battery life prediction. To achieve this objective, researchers have made improvements to existing mechanistic models to further consider microelectrode morphology. Roder et al. [96] established a particle-size distribution (PSD) model to investigate the influence of the PSD of active materials on the performance of graphite electrodes. The surface overpotential and uneven reaction rates caused by particle heterogeneity are revealed through analyzing the charging behavior of electrode particles under different local current densities. Furthermore, Kirk et al. [97] designed a unimodal PSD and a bimodal PSD based on the PSD model. Their simulations demonstrated the equivalence between the unimodal PSD model and the SPM model and the advantage of the bimodal PSD model in fitting experimental data. Sharma et al. [98] employed Computational Fluid Dynamics (CFD) methods to simulate the mass transport processes within the morphology of real electrodes. This approach enabled them to obtain closer approximations to the actual concentration variation processes within electrodes. Dai et al. [99] constructed a battery charging and discharging model capable of considering arbitrary electrode morphologies through a hybrid modeling approach combining CA and PDEs. In this model, irregular phase boundaries or moving phase interfaces were described using CA, while the conservation of mass and energy in the physical field was captured by PDEs. This method leveraged the strengths of both modeling techniques to efficiently model different processes, thereby achieving the efficient operation of each component of the model. A schematic diagram of different mechanism models for LIBs is shown in Figure 3, and the strengths and limitations of different models are summarized in Table 2.

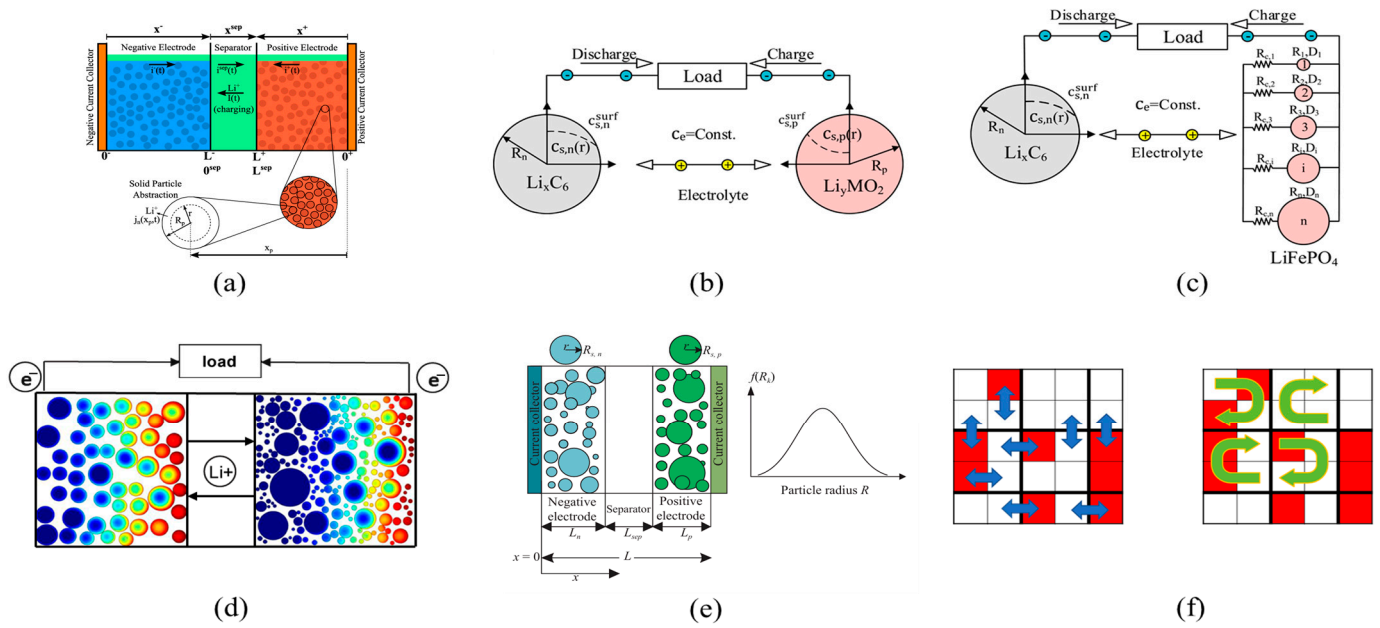


**Figure 3.** Schematic diagram of different mechanism model for LIBs: (a) P2D model [37]; (b) SPM model [100]; (c) MPM model [100]; (d) PSD model [101]; (e) CFD model [102]; (f) CA model [103].

**Table 2.** A summary of strengths and limitations of different LIB models.

Model	Overview	Strength	Limitation
P2D	Under the assumption of the uniform distribution of spherical particles, the liquid-phase variables are calculated along the $x$ direction, while the solid-phase variables are calculated along the $r$ direction.	It is capable of considering the influence of porosity and particle size, while maintaining a moderate calculation efficiency.	It cannot consider the non-uniform distribution and irregular nature of particles, and the calculation speed may not satisfy the requirements for electrode structure optimization and online applications.
SPM	The cathode and anode in the P2D model are simplified to a single spherical particle.	It has the highest computational efficiency among electrochemical models.	The computational accuracy decreases significantly under high-current charging and discharging conditions, and it fails to consider the influence of porosity.
MPM	It is equivalent to the coupling of multiple SPMs, in which both the cathode and anode are considered to be composed of particles of various sizes.	Featuring moderate computational efficiency, it also incorporates a degree of consideration for the distribution information of electrode particles.	The influences of porosity and particle position distribution cannot be considered.
PSD	A further improvement of the MPM, in which the influence of particle-size distribution on battery operational mechanisms is incorporated.	The PSD model is capable of considering various particle-size distributions, enabling a more detailed investigation into the influence of electrode particle sizes on battery performance.	The influence of particle position distribution cannot be considered.

Table 2. Cont.

Model	Overview	Strength	Limitation
CFD	Considering mass transfer and reaction processes in electrodes with arbitrary morphologies.	It enables the visualization of the spatio-temporal evolution of variables, and the construction and evaluation of electrodes with arbitrary shapes and morphologies.	The computational efficiency is generally low.
MSMD	Interacting with the averaged values of variables across different scales to achieve multi-scale modeling.	By correlating the particle scale, electrode scale, and battery scale, it enables the exploration of the interaction mechanisms among variables across different scales.	Using only averages for interaction enhances computational efficiency but results in the loss of spatial distribution information.
CA-FD	A hybrid approach for LIB modeling, in which CA is adopted to describe reaction–diffusion processes and FD methods are used to calculate potential distributions	Capable of considering electrodes with arbitrary morphologies and featuring a high computational efficiency.	The selection of time steps for the two parts of the model requires exploration to find a matching time step that maintains the rationality and accuracy of the step-by-step calculations.

In addition, a logic diagram for the mechanism models is shown in Figure 4; from left to right, the lower the computational efficiency of the model, the more information inside the electrode is considered. Researchers can choose the model type according to their requirement.

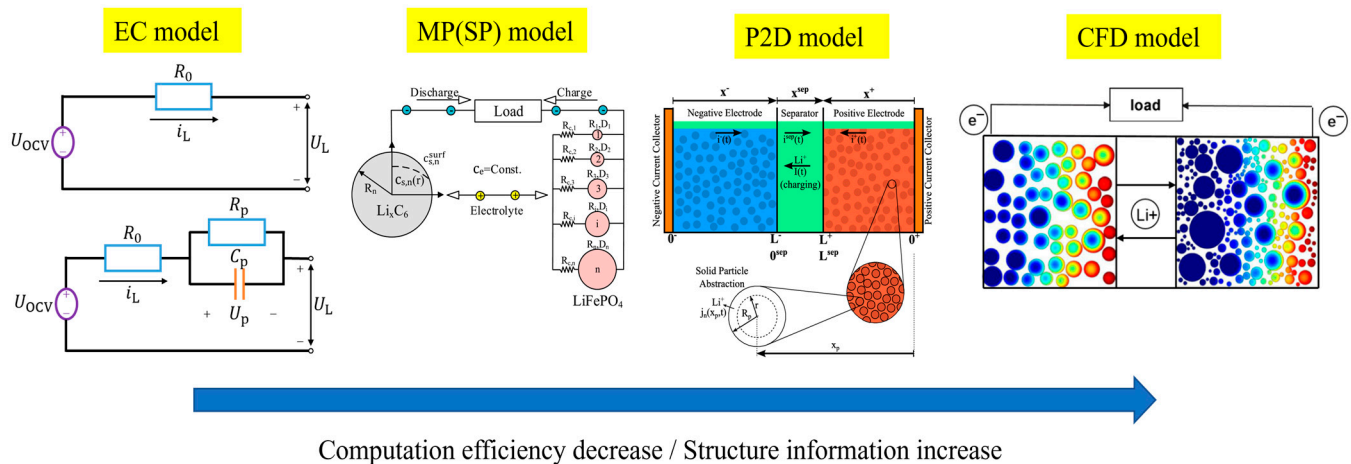


Figure 4. The logic diagram of mechanism models.

### 2.3. The Incorporation of Battery Aging in Long-Cycle Modeling of LIBs

Currently, the expected lifespan of electric vehicles ranges from 10 to 15 years, with the durability of LIBs being the primary limiting factor. To facilitate the better understanding of the battery aging mechanism, the main aging mechanisms within LIBs, as well as the positive feedback mechanism in the aging process of LIBs, are summarized in Figures 5 and 6. Generally, battery aging in LIBs encompasses capacity loss, impedance increase, and power degradation. Understanding the characteristics of battery aging could facilitate the development of reliable battery management systems, thereby enabling accurate predictions of battery life and remaining capacity. The primary aging mechanisms of LIBs include the formation and growth of Solid Electrolyte Interface (SEI), the deposition of metallic lithium at the anode, mechanical fracture of electrode materials, and the consumption of

electrolytes and additives, etc. This section delves into the specific aging mechanisms and their considerations in mechanistic modeling.

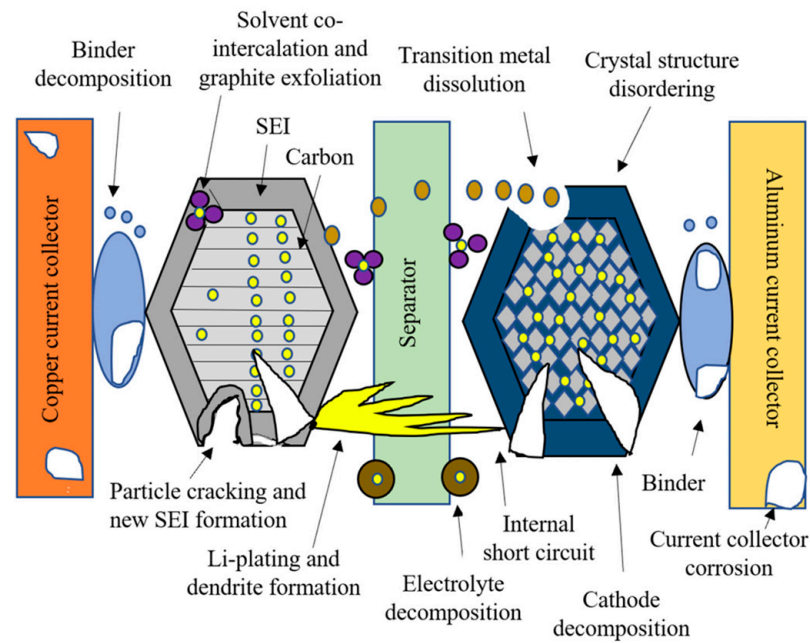


Figure 5. Main aging mechanisms within LIBs [104].

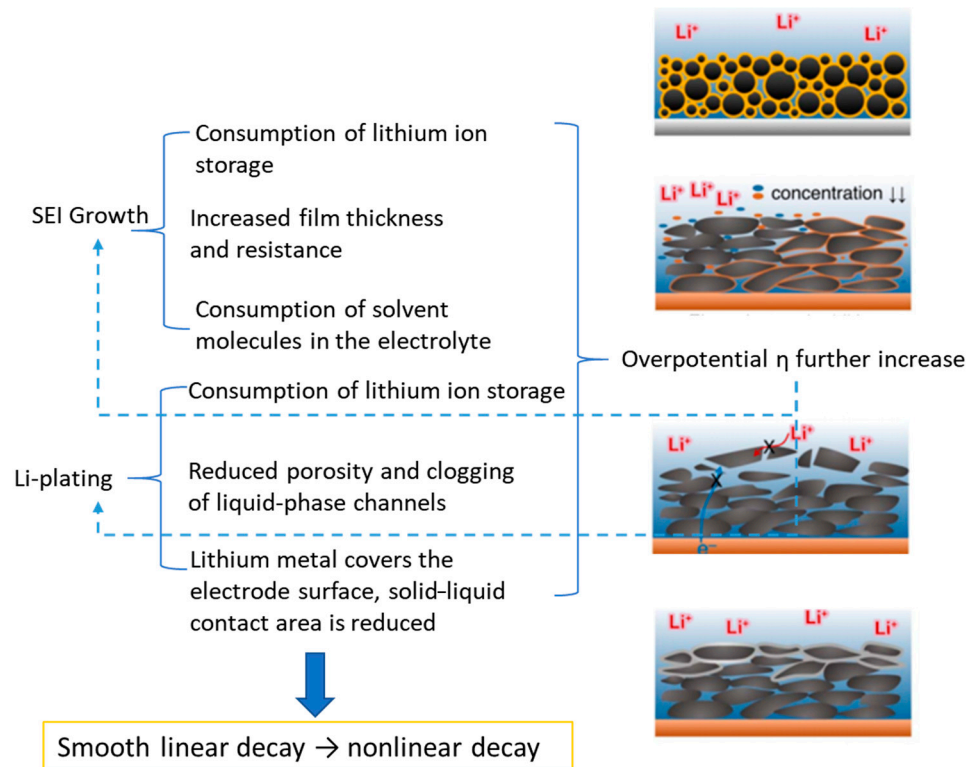


Figure 6. The positive feedback mechanism in the aging process of LIBs [105].

### 2.3.1. Side Reactions Involved in the Growth of SEI Layer

The SEI is defined in the literature as a porous film structure that forms on the surface of electrode materials during the initial charging process. Its primary function is to prevent further reactions between the electrode and electrolyte while enabling the transmission

of lithium ions through the film to reach the electrode surface, thereby facilitating normal lithium-ion extraction/insertion during the charge–discharge process. However, due to the porous nature of the SEI, after its initial formation during the first charge, a small amount of electrolyte continues to diffuse into the SEI and diminish at the electrode surface, leading to a gradual thickening of the SEI layer. This, in turn, results in the loss of active lithium ions. It is generally recognized that the capacity fade attributed to SEI growth exhibits a linear or square root dependence on the number of cycles, as the increasing thickness of the SEI slows down the diffusion speed of lithium ions within the film.

The capacity fade of LIBs due to the SEI film has been investigated in numerous mechanistic models, and the formation and growth of the SEI have also been extensively studied. Spotnitz et al. [106] developed a mathematical model to investigate the impact of the acid-induced erosion of the SEI layer on the capacity loss of LIBs. Liu et al. [107] established an electrochemical–thermal model based on the diffusion process of solvents through the film and the reaction kinetics at the interface. They hypothesized that the SEI grows faster during charging processes than discharging processes, and temperature increases accelerate SEI growth, leading to increased capacity loss in LIBs. Guan et al. [108] constructed a two-dimensional phase-field model to simulate the microstructural evolution during SEI growth and predicted the growth rate of SEI thickness. Xie et al. [109] discovered that the assumed operating conditions of LIBs play a crucial role in capacity decay, with higher charge–discharge rates accelerating capacity loss. Kim utilized molecular dynamics to study the influence of electrolyte formation on the SEI layer [110]. Ramadass et al. [111] built a capacity loss model for LIBs that incorporates solvent reduction reactions, in which the SEI growth is assumed to be primarily concentrated in the interlayer region and is a weak function of cycling conditions. Prada et al. [112] found that the capacity loss of LIBs is a function of SEI formation and temperature. Tan et al. [113] also studied the formation of the SEI on the anode of LIBs and indicated that a significant amount of lithium is lost during SEI formation. Sungjemmenla et al. [114] reviewed research progress in preparing a stable SEI from aspects such as the use of electrolyte additives, artificial engineering, and cathode heteroatom doping. They pointed out that computational modeling is needed to qualitatively and quantitatively predict the formation and degradation mechanisms of the SEI in order to understand the interface’s formation and evolution.

### 2.3.2. Side Reactions of Lithium Deposition

The capacity fade of batteries exhibits an exponential increase phenomenon after multiple cycles. Schuster et al. [115] conducted a study on a set of 1.95 Ah commercial 18,650 batteries under a constant temperature and charging rate. During the initial stages, the capacity fade and impedance increase exhibited a linear relationship with the number of cycles, with the growth of the surface SEI layer being the primary aging mechanism. However, after prolonged cycling, the battery capacity decreased sharply, and the battery impedance increased drastically, indicating that some other mechanism had dominated the aging process. On this basis, key features of the nonlinear aging phenomenon can be summarized.

It first occurs in various LIBs using lithium oxide-based cathodes, including lithium iron phosphate, lithium manganese oxide, and lithium cobalt oxide. Additionally, the loss of lithium ions primarily occurs at the anode. Through energy-dispersive X-ray spectroscopy analysis of severely aged batteries, a thick film was observed near the anode/separator interface, while the cathode material showed no significant morphological changes. Therefore, it is reasonable to assume that this nonlinear aging behavior is closely related to the mechanism of lithium-ion insertion into the anode. Klett suggested that a significant amount of metallic lithium exists within the SEI layer at the anode/separator interface, leading to the conclusion that the nonlinear battery aging after prolonged cycling is caused by lithium deposition reactions [116]. The equilibrium potential for lithium insertion into graphite is quite close to that for lithium deposition reactions. Consequently, these two reactions compete during battery charging. Under a high current or near the

end of charging, the solid–liquid phase potential difference at the anode becomes negative, leading to lithium deposition instead of intercalation. Plated lithium can react with the electrolyte to form a new SEI layer or become isolated from the electronically conductive matrix, resulting in a loss of lithium inventory. Furthermore, plated lithium metal may form dendrites, which, in the worst-case scenario, can puncture the separator, causing internal short circuits and potentially hazardous consequences [117].

With respect to the Li/Li<sup>+</sup> potential as the reference, the insertion potential of Li in graphite ranges from 65 to 200 mV. When the local potential of the anode becomes negative, the process of lithium ions being reduced to metallic lithium at the graphite anode is thermodynamically feasible, known as lithium deposition [118]. The overpotential generated by polarization is primarily composed of ohmic overpotential, charge transfer overpotential, and diffusion overpotential, which are the kinetic causes of lithium deposition. Experimentally, it is challenging to distinguish between these three overpotentials [119], but simulations can be used to calculate the overpotential, which serves as a kinetic condition for lithium deposition. Lithium deposition occurs when the sum of the equilibrium potential and overpotential is negative relative to Li/Li<sup>+</sup>. Lithium deposition and intercalation/deintercalation reactions occur in parallel, with lithium ions being inserted and deposited during charging, and deintercalated and stripped during discharging. However, some inactivated lithium cannot be stripped, while some deposited lithium strips to form new active lithium. Thus, lithium deposition is partially reversible, occurring in LIBs with different cathode materials (NCM [115], LCO [117], LFP [120]). The occurrence of lithium deposition is determined by the interplay of charging rate, temperature, and State of Charge (SOC), with lower temperatures, higher rates, and higher SOCs more prone to promoting lithium deposition [121]. Even under relatively mild conditions, lithium deposition may occur, due to factors such as reduced anode porosity and weakened ion transport caused by SEI growth [122]. Consequently, the decline curve becomes highly nonlinear in the later stages of long-term cycling or high-current charging and discharging, representing the second stage primarily dominated by lithium deposition. Depending on the trend of this second stage, it can be further classified into accelerated, decelerated, or linear decline, all primarily caused by lithium deposition [122]. Pankaj et al. [123] employed the BV equation to describe the kinetics of lithium deposition side reactions and argued that the lithium deposition reaction is partially reversible. Yang et al. [124] proposed an aging model for lithium-ion batteries that considers SEI film growth and lithium deposition side reactions, in which the aging results of NCM batteries under prolonged cycling under moderate operating conditions were investigated. The research indicates that battery aging is linear during the initial cycling stage, primarily driven by SEI film growth, while it becomes highly nonlinear towards the end of cycling. The transition from linear to nonlinear aging is dominated by lithium deposition.

### 2.3.3. The Consumption of Electrolytes and Additives

Aging or disintegration of active materials (primarily referring to cathodes) is also a crucial factor contributing to the capacity fade of LIBs. Possible reasons for the dissolution of cathode materials include acid erosion, material structural defects, overcharging, and high-rate charging. Aurbach et al. [125] conducted a study on the capacity fade of LiCoO<sub>2</sub> intercalation electrodes, in which the formation of cathode surface films and cobalt dissolution at different temperatures were analyzed. It was concluded that the capacity fade of LiCoO<sub>2</sub> electrodes is primarily due to changes in electrode surface morphology rather than bulk degradation. Therefore, increasing the electrode surface area/solution volume can reduce the losses caused by electrode disintegration. Wu et al. [126] investigated the capacity loss and cycling performance of LiMn<sub>2</sub>O<sub>4</sub>/C batteries under alternating temperature and vibration operating conditions. The experiments revealed that the batteries exhibit a faster capacity decay under these conditions compared to a constant temperature due to the reduced crystallinity of LiMn<sub>2</sub>O<sub>4</sub>, increased lattice constants, and enhanced Mn dissolution, which accelerate capacity loss. Additionally, as the number of cycles increases,



the surface film on the battery anode is damaged, leading to decreased thermal stability. This damage to the surface film also accelerates its repair rate, further increasing internal impedance and capacity loss. Fang et al. [127] first confirmed during cycling that Ni and Mn deposit on the anode surface when  $\text{LiNi}_{0.5}\text{Mn}_{1.5}\text{O}_4$  is used as the cathode material. Since the conductivity of metallic Ni and Mn is inferior to  $\text{Li}^+$ , this increases impedance and causes capacity decay. Yoon et al. [128] studied the capacity fade mechanism of lithium-ion batteries with silicon nanoparticles as the anode and concluded that capacity loss stems from incomplete de-lithiation during charging and discharging. They suggested that the remaining capacity can be enhanced by reducing the cut-off voltage for de-lithiation or adding electrolyte additives.

The dissociation of electrolytes is another factor that affects capacity fade. Solids generated from side reactions may adhere to electrode surfaces, hindering lithium-ion intercalation/deintercalation and increasing electrode interface resistance. Electrolyte reduction also consumes lithium salts and solvents, altering electrolyte concentration and potentially generating gases, posing safety risks. Markevich et al. [129] analyzed the capacity fade of batteries using  $\text{LiCoPO}_4$  as the cathode and  $\text{LiPF}_6$  as the electrolyte and found that the nucleophilic attack of  $\text{F}^-$  from HF formed by electrolyte dissociation on  $\text{P}^-$  leads to the cleavage of phosphorus–oxygen bonds and the formation of  $\text{LiPO}_2\text{F}_2$  salts soluble in the electrolyte, which further damages the electrode surface structure, causing capacity loss. Wu et al. [130] studied the relationship between battery voltage and the electrochemical stability of electrolytes and discovered that higher battery voltages promote oxidative decomposition reactions between the electrolyte and cathode materials. Apart from common SEI and lithium deposition side reactions, ester exchange and polymerization reactions occur in organic solvents within the electrolyte. Conductive salts such as  $\text{LiPF}_6$  will degrade during the reaction to generate organic phosphates and fluorides. Henschel et al. [131] constructed a lithium battery model based on Support Vector Machines (SVM) to analyze the aging of five commercial lithium-ion battery electrolytes. The results indicated that both energy-type and power-type batteries experience varying degrees of electrolyte depletion as their capacities decline, with a significant drop in  $\text{LiPF}_6$  concentration.

Generally, model-based methods can achieve a high precision in LIB modeling. However, in the process of model construction, both the selection of model types and the acquisition of model parameters require a high level of experience and knowledge from the operators in this field. Additionally, the finally obtained mechanistic models are often not universally applicable across different types of batteries, which limits their practical application in industry.

### 3. Data-Driven Modeling for LIBs

Although the structure–effect mechanism of batteries can be reflected in the aforementioned electrochemical models, they still suffer from complexity and unmeasurable internal parameters, making it challenging to integrate them with real electrodes. For instance, the estimation of the actual battery operating state based on the mechanistic model necessitates rapid convergence to facilitate online parameter identification and state estimation. With advancements in data acquisition and AI technology, data-driven models have emerged as the preferred method for battery modeling and have been widely applied in BMS [132–134]. Generally, the main applications include fault diagnosis and health management, cell monitoring, cell balancing, state estimation, charge and discharge control, and thermal management [135]. Under this scope, a total of 68 papers published within the last five years were investigated, which are summarized in Figure 7. It can be observed that battery state estimation is an important research focus and also the most key feature within the application of BMS. Therefore, the estimation of battery state is regarded as an emphasis in this section discussing data-driven models. The battery state represented by State of Health (SOH), State of Charge (SOC), and Remaining Useful Life (RUL) reflects the ratio of the battery's maximum available capacity at the current moment to its capacity in a fresh state. This metric serves as feedback on the battery's performance after extended

cycling, enabling the quantification of the degree of internal aging of the battery at any given time. Based on an accurate acquisition of the battery’s operational status, the BMS could regulate the operational parameters of vehicle batteries, ensuring that they operate within a reliable safety range while meeting driving requirements, thereby extending the battery’s service life.

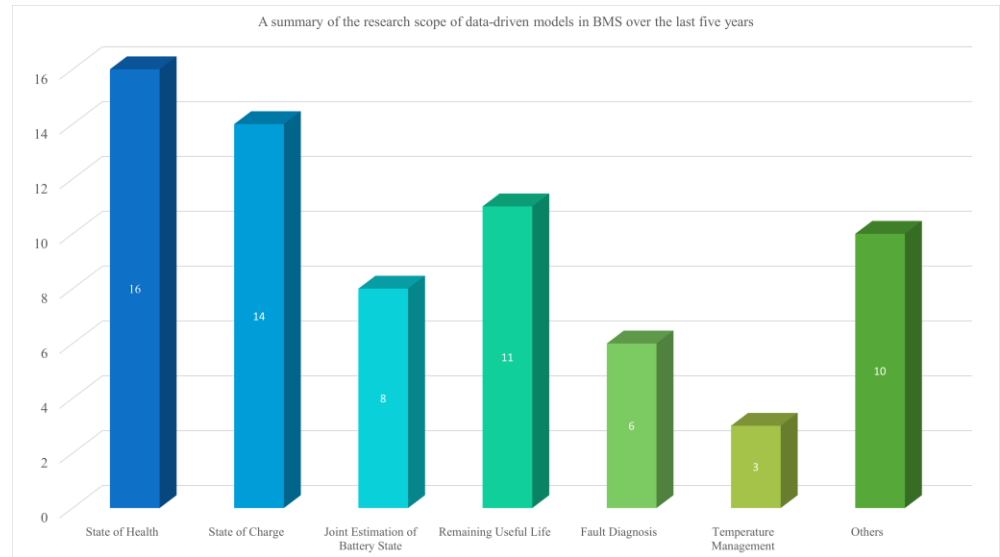


**Figure 7.** A summary of the research scope of data-driven models in BMS over the last five years.

The degradation of LIBs is a nonlinear and dynamic electrochemical process [136,137], and data-driven methods aim to extract the nonlinear and dynamic characteristics from historical aging process data for the purpose of estimating the battery state. A well-trained data-driven model based on extensive and high-quality process data can typically be employed for online estimation of the battery state [18]. It can achieve a high estimation accuracy without the need to consider the underlying process mechanisms. The generic framework for data-driven LIB modeling is illustrated in Figure 8.

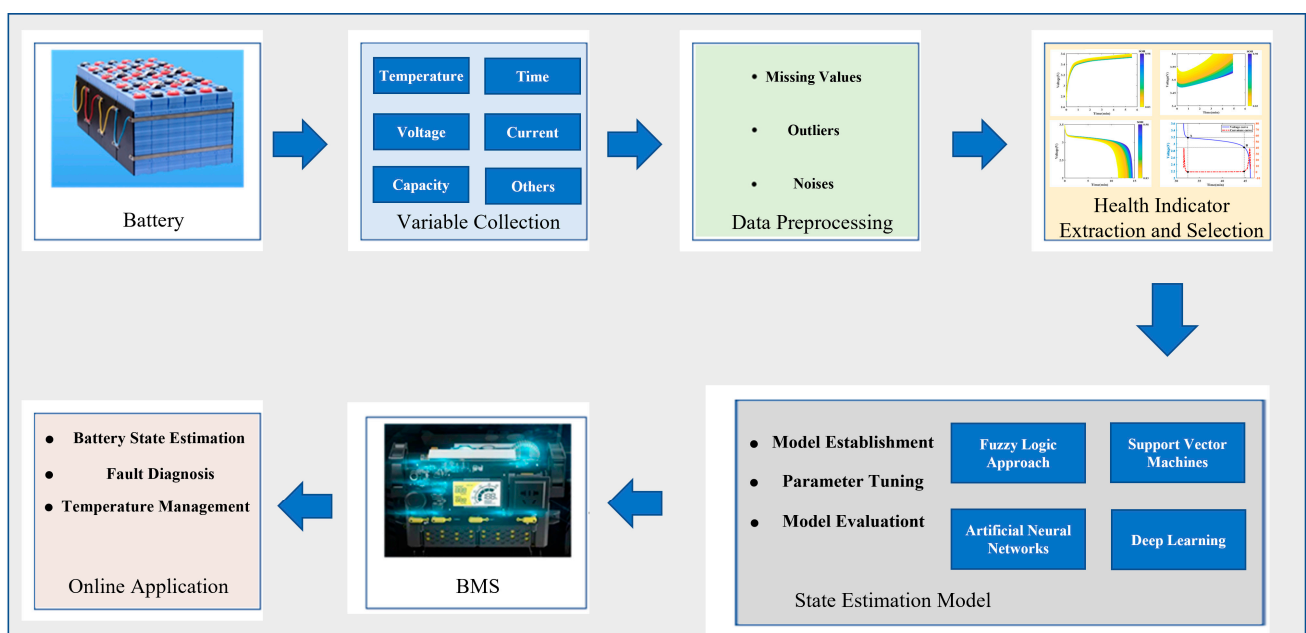


**Figure 8.** The generic framework for data-driven estimation of battery state.

### (1) Data collection and preprocessing

The first step involves the data collection and preprocessing. Data related to the battery aging process are collected from sensors, including variables such as current, voltage, internal resistance, impedance, and maximum available capacity. Then the data preprocessing has to be conducted because the raw data may contain outliers and missing values. Moreover, during the process of meter acquisition and signal transmission, the data inevitably suffer from various types of noise interference. Therefore, data denoising is typically performed on the raw data. Common data denoising methods primarily involve filtering techniques, which include both time-domain smoothing methods like a moving average [138] and weighted moving average [139], as well as signal time–frequency analysis methods including Fourier Transform [140], Short-Time Fourier Transform [141], wavelet transform [142], and empirical modal decomposition [143].

### (2) Health indicator extraction and feature selection

The next step is the extraction of battery health indicators, which usually include fundamental process features such as the denoised current and voltage, as well as derived features extracted from these baseline features. Examples of derived features include the average battery temperature across each cycle, the peak point of the first-order moment of the voltage curve, the peak points on the incremental capacity curve, and the peak points on the differential voltage curve. Given the complex nonlinear electrochemical environment within batteries, the simplified features like denoised current and voltage alone are insufficient to support the high-precision estimation of the battery state through data-driven methods. Consequently, a more targeted extraction of health indicators is necessary for the denoised data. Under varying charging and discharging conditions, batteries exhibit distinct effective curve characteristics, which require a context-specific approach for health indicator extraction. Current research often relies on empirical methods for simplistic feature extraction [144–146], while the extraction of features relevant to battery state estimation from raw data has been an attractive research focus in recent years and will be further discussed in Section 3.2.

Moreover, the extracted health indicators may not always be mathematically correlated with the battery's state, which could lead to redundancies that can increase model complexity and decrease prediction accuracy. Hence, feature selection is also a crucial and indispensable step in data-driven LIB modeling. The relevant studies on feature selection will be introduced in Section 3.3.

### (3) Feature extraction for battery state estimation

The last step is to utilize the battery health indicator obtained from the aforementioned steps to construct a data-driven model to extract critical internal features for battery state estimation. This part of the study is usually oriented towards differences in algorithms to capture various factors reflected in process data during battery degradation process [5,147,148]. Generally, data-driven feature extraction methods for LIB modeling are categorized into filtering techniques, Stochastic Processes, and AI [137]. Among these methods, filtering techniques, often implemented using Kalman Filters [149,150], typically rely on state–space equations and involve simplifications such as assuming the battery is discharging at a constant temperature and current, which deviate from the actual operation process of lithium batteries, resulting in significant discrepancies between predicted and actual values. Stochastic Processes, on the other hand, can better characterize the degradation processes of lithium batteries. However, they often overlook the influence of a time-varying environment, randomly varying currents, self-recharge characteristics, and system configurations during battery operation, and their computational complexity is relatively high [137]. With the advancement in computer technology and the popularity of artificial intelligence, massive attractive ML algorithms have been proposed for extracting various complex data features [151–156]. These methods span statistical models and machine learning models to deep learning models. They are computationally efficient, do not require prior knowledge or experience-based modeling, and exhibit strong capabilities in capturing the nonlinear and time-varying characteristics

of battery degradation processes. Consequently, they have emerged as the most extensively researched and widely applied methodologies. A detailed introduction to ML-based feature extraction algorithms will be provided in Section 3.4.

### 3.1. Public Database for LIB Modeling

Data-driven models do not require a precise process mechanism or prior knowledge of the battery aging process, but high-quality training datasets are an important prerequisite for data-driven models to achieve high estimation accuracy and generalization performance. Therefore, battery cycling test datasets are becoming increasingly important with the demand for the development of data-driven models. The data collected during the charging and discharging process of a battery, as well as the assessment of the battery's performance and degradation over time, contain important information regarding the battery's behavior [157]. The open battery-cycling database stands out prominently due to its invaluable contribution of detailed cycling data for a broad spectrum of commercial LIBs. Such a rich resource facilitates the development, refinement, and validation of battery models and algorithms, while also promoting standardization in battery testing methodologies and reporting practices. This standardization is paramount for advancing the field and fostering the creation of more efficient and reliable battery systems. Several commonly used open datasets for LIB modeling are summarized in this section, in which the main characteristics of batteries, the data sources, and their applications and purposes are presented to provide a reference for readers.

#### (1) MIT dataset

The MIT dataset [158] primarily comprises laboratory-scale cycling test data of 124 APR18650M1A batteries under a constant ambient temperature of 30 °C. These batteries are grouped into three distinct batches, "2017-05-12", "2017-06-30", and "2018-04-12", each with a nominal capacity of 1.1 Ah and a nominal voltage of 3.3 V. During testing, various fast-charging strategies are implemented for different batteries, as illustrated in Figure 9. Q1 denotes the charging status when batteries switch from C1 to C2. During the SOC ranging from 80% to 100%, all batteries adopt a constant current–constant voltage (CC-CV) charging strategy, with a charging rate of 1C (i.e., 1.1 A), a cut-off voltage of 3.6 V, and a cut-off current of C/50. Additionally, all batteries share the same discharging conditions, following a strategy that initially maintains a constant current and then transitions to constant voltage, with a corresponding discharging rate of 4C and a cut-off voltage of 2.0 V. Information regarding the five batteries from this dataset is detailed in Table 3, where cycle life refers to the number of charge–discharge cycles required for the battery's health state to degrade from its initial state to 80% of its original capacity.

**Table 3.** A brief overview of batteries in the MIT dataset.

Encoding	Charging Strategy	Channel	Cycle Life
EL150800460623	3.6C(80%) – 3.6C	3	1177
EL150800464977	4.0C(80%) – 4.0C	5	1226
EL150800464883	4.4C(80%) – 4.4C	7	1074
EL150800465027	4.8C(80%) – 4.8C	9	870
EL150800464002	5.4C(80%) – 5.4C	11	534

#### (2) NASA dataset

The NASA dataset provides six files in the Matlab2016B data storage format, as summarized in Table 4. These files contain nine groups of battery samples, with each group consisting of 3 or 4 individual battery samples, totaling 34 individual batteries in all. These six battery sets differ in terms of their depth of discharge, discharge rates, and ambient temperatures. The dataset can be downloaded at <https://www.nasa.gov/content/prognostics-center-of-excellence-data-set-repository> (accessed on 1 December 2023).

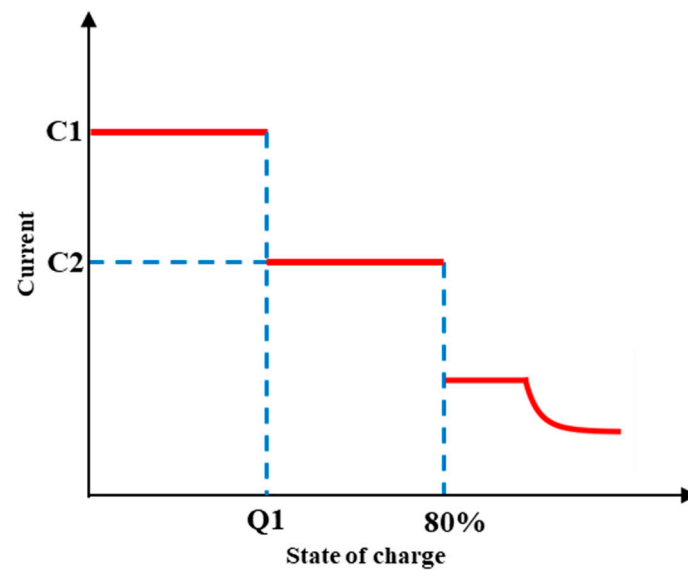


Figure 9. Schematic diagram of fast-charging strategy [159].

Table 4. A brief overview of six data files in the NASA dataset.

No.	Name	Encoding
1	BatteryAgingARC-FY08Q4	B0005–B0007, B0018
2	BatteryAgingARC_25_26_27_28_P1	B0025–B0028
3	BatteryAgingARC_25-44	B0025–B0034, B0036, B0038–B0044
4	BatteryAgingARC_45_46_47_48	B0045–B0048
5	BatteryAgingARC_49_50_51_52	B0049–B0052
6	BatteryAgingARC_53_54_55_56	B0053–B0056

### (3) Center for Advanced Life Cycle Engineering (CALCE) dataset

The CALCE dataset was proposed by a research team at University of Maryland, and it can be downloaded at <https://calce.umd.edu/battery-data> (accessed on 1 December 2023). The CALCE dataset offers test data for a total of six types of batteries, including cylindrical batteries such as INR 18650-20R and A123, prismatic batteries like CS2 and CX2, pouch cells denoted as PL, and other types of batteries labeled as K2. Among these batteries, the test data for prismatic batteries CS2 and CX2 can be utilized to conduct remaining life prediction. The CALCE dataset characterizes the performance of LIBs through parameters such as voltage, current, resistance, and battery capacity. These parameters are also influenced by ambient temperature and experimental testing procedures. Among them, the primary focus remains on battery capacity. Taking the CS2 battery as an example, it has a rated capacity of 1.1 Ah. All CS2 batteries undergo a similar charging process, adhering to a standard CC-CV protocol. The constant current rate is either 0.5 C or 1 C and continues until the voltage reaches 4.2 V, whereupon the voltage is maintained at 4.2 V until the charging current drops below 0.05 A. Ordinarily, the discharge cut-off voltage for these batteries is 2.7 V. Overall, the CALCE battery dataset has a relatively small number of individual battery samples per group, with a maximum of four samples per group. Compared to the NASA dataset, each individual battery in the CALCE dataset has a relatively abundant number of sample points, approaching 1000 sample points. However, the overall degradation trends of the capacity degradation curves exhibit similar characteristics.

### (4) Oxford Dataset

The Oxford Battery Degradation Dataset comprises eight Kokam (SLPB533459H4) Li-CoO<sub>2</sub> lithium-ion pouch cells with a rated capacity of 740 mAh. These cells feature cathodes made from lithium cobalt oxide and lithium cobalt nickel oxide, and anodes made from graphite. The cells are labeled as Cell1 through Cell8. The cycling aging tests for these cells

were conducted in a temperature chamber set at 40 °C. The experiments employed a CC-CV charging mode and simulated the dynamic discharge patterns of the Urban Artemis electric vehicle during actual driving conditions. Following this, charge–discharge tests were performed every 100 aging cycles until the battery life reached the aging threshold. Throughout the experiments, an 8-channel Big-Logic MPG-205 experimental instrument was used to record data such as cycle number, time (t), current (740 mA), voltage (V), temperature (°C), and charge (q) during the charge–discharge process. Additionally, researchers recorded Open Circuit Voltage (OCV) data for fitting the OCV-SOC curve. The dataset, as well as a detailed description, can be referred to at <http://howey.eng.ox.ac.uk/data-and-code/> (accessed on 1 December 2023).

The four datasets introduced above are commonly used in current research to validate and compare newly proposed data-driven battery state estimation algorithms. In addition to these datasets, several other lithium-ion battery datasets have been publicly released by research institutions and industries in recent years, including the Cambridge University and Faraday Institution dataset [160], the Sandia dataset [161], and the Huazhong University of Science and Technology (HUST) dataset [162], etc., which further enrich the data resources for advancing the development of machine learning algorithms in battery state estimation research.

### 3.2. The Extraction of Health Indicators for LIBs

As mentioned before, the information provided by raw charging and discharging curves is inherently limited, which poses challenges in the accurate estimation of battery state solely through these curves. However, by extracting health indicators related to the battery's maximum available capacity from these curves, more comprehensive information can be obtained [23]. Depending on the form of feature extraction, health indicators can be classified into basic indicators and secondary indicators. Basic indicators refer to those that can be directly obtained from raw current, voltage, and temperature profiles, such as the time difference corresponding to the same voltage range in a voltage profile [163] and the peak value of a temperature profile [158].

Xiong et al. [164] collected aging data from eight second-life LIBs and observed that during the constant current charging phase, batteries with varying degrees of aging exhibit different changes in charge capacity within the same voltage range in the voltage–time curve. They subsequently divided the voltage range into eight segments and extracted the corresponding capacity changes in each segment as health indicators. Beyond segmenting the voltage range, Guo et al. [145] calculated the capacity difference between the first and the 100th voltage segment, and their results demonstrated a linear correlation between this capacity difference indicator and battery SOH.

It is worth noting that laboratory-scale tests often involve full charging and discharging cycles, whereas in practical applications, traction batteries are rarely fully discharged, which can impact the CC charging phase of the subsequent cycle. Therefore, Liu et al. [146] collected aging data from four LIBs under CC-CV charging conditions. They extracted various health indicators, including charging time, charging capacity, average current, and time differences corresponding to each current range during the CV charging phase. The results revealed that eight out of the nine extracted indicators exhibited strong linear correlations with battery SOH.

Given the limited information reflected by basic health indicators, secondary indicators have been introduced, which employ mathematical transformations such as differentiation [165,166] for aging indicator extraction. Incremental Capacity Analysis (ICA) [167–169] is a commonly used method for extracting health indicators. By differentiating the charge capacity difference and terminal voltage difference for each cycle, the voltage curve can be converted into an incremental capacity (IC) curve with a series of peaks and valleys. The IC curve reflects an increase in battery power per unit voltage and can be used to detect electrochemical changes caused by capacity loss [170]. The regular changes in the positions of IC peaks and valleys for different aging levels can be leveraged to estimate the health

state of LIBs. Weng et al. [171] determined the ordinate of the peak points on the differential curve as an aging indicator through the ICA method. The effectiveness of this indicator was validated on eight batteries with a prediction error of less than 1%. Wen et al. [172] conducted cycle charge–discharge tests on five 18650-type LIBs and identified the abscissa, ordinate, and peak slope of the IC curve as health indicators for SOH estimation, achieving an average prediction error of 1.16%.

Furthermore, Goh et al. [173] observed regular changes in curvature within the discharge curve and proposed a novel health indicator extraction method based on the U-shaped curvature. By dividing the curve into three sections based on curvature, they extracted the time difference, voltage difference, area under the curve, and abscissa and ordinate of the endpoints in the plateau section as health indicators. The effectiveness of this method was validated in a machine learning model, achieving a mean absolute error of less than 1.08%. Tao et al. analyzed the battery aging mechanism and the changing law of the curves and extracted a total of 61 health indicators related to performance degradation from the cycling curves [159]. In summary, the selection of health indicators plays a crucial role in improving the prediction accuracy of data-driven models. Extracting health indicators solely based on fundamental curve patterns is limited, and performing a secondary indicator extraction based on these foundational curves to obtain valuable indicators that underly mechanisms of battery behavior is vital for enhancing prediction accuracy.

### 3.3. Feature Selection

The extracted health indicators need not be mathematically correlated with the battery state to be estimated. Part of them could be highly correlated with the estimation target, while others may have poor correlations. Moreover, the health indicators that are highly related with battery health state could also be redundant with each other. Using all health indicators directly for machine learning modeling not only increases the model complexity but also decreases the estimation accuracy, and is prone to causing overfitting [174]. Feature selection methods play an important role in classification or regression tasks to save computational costs, refine the size of the dataset, and improve the operational efficiency and estimation accuracy of machine learning methods [175].

Generally, feature selection methods are categorized into filter-based methods, wrapper-based methods, and fusion-based methods [176]. In summary, the primary target of feature selection is to identify a subset of the most relevant features, while minimizing redundancy among them. Correlation analysis approaches are commonly used in machine learning to evaluate the degree of correlation between features and the prediction target. The Pearson correlation coefficient is the most classic method for correlation analysis, which is capable of evaluating the linear relationship between features and the target. Considering that the battery aging process is a nonlinear process, certain related features may not be effectively identified by linear approaches. For nonlinear relationships, information theory, represented by Mutual Information (MI), demonstrates significant advantages by estimating the shared information content between variables through the estimation of their joint distributions [177]. However, a limitation is that there is no upper limit for the MI value, and there is no threshold for the MI to determine whether the correlation is significant. To address this limitation, Ji et al. suggested estimating the threshold of MI through random sequences generated by the Monte Carlo method [178]. Estevez et al. proposed a normalized MI to standardize MI to between 0 and 1 [179]. On this basis, Reshef et al. further proposed a maximal information coefficient to improve the estimation precision of MI in big datasets [180]. The above studies focus on the calculation of correlation, while the redundancy is hard to characterize. Information theory also provides the theoretical foundation for the calculation of redundancy. The max-relevance and min-redundancy criteria has been widely adopted in information theory for feature selection [181]. Bennasar et al. [182] proposed joint MI maximization to measure the importance of candidate features using a conditional MI. Xiao et al. [183] proposed a max-relevance and min-redundancy method based on neighborhood MI. Yin et al. [184] proposed a maximum dynamic rele-

vancy, minimum redundancy-based feature selection algorithm. Che et al. further proposed a maximum relevance, minimum common redundancy feature selection method, which comprehensively considers the redundancy among candidate features [185]. Through the evaluation of relevance and redundancy, the importance of candidate features can be systematically ranked, and the optimal feature subset can be further determined through the assessment of information gain of the target variable [186].

### 3.4. Feature Extraction by ML Algorithms

After determining the optimal subset of extracted health indicators, the feature extraction is a critical step to capture useful information to achieve an accurate and real-time estimation of the battery health state. As one of the dominant data-driven methods, ML technology, mainly including linear regression, Support Vector Regression (SVR), Gaussian process regression (GPR), and deep learning, etc., has garnered a widespread application in the realm of such regression task.

Linear regression, represented by partial least squares regression and Gaussian process regression [187], exhibits notable advantages in terms of computational efficiency, model interpretability, and generalization ability. However, linear models are usually overly simplistic and thus inadequate for capturing the intricate nonlinear features inherent in battery degradation processes. The SVR is an effective supervised learning approach that introduces kernel functions to transform low-dimensional data into a higher-dimensional space, where the nonlinear relationships between inputs and outputs can be extracted. Nuhic et al. [188] proposed a novel data-driven strategy that combines collected feature signals such as capacity and temperature as inputs into an SVR model to achieve an accurate prediction of battery SOH. To facilitate online estimation of the battery health state, Klass et al. [131] applied standard battery tests conducted in a laboratory and parameters collected from regular EVs to an SVR model, and the effectiveness of the SVR model was demonstrated through comparing the estimated SOH indicators with those measured directly. Meng et al. [189] conducted current pulse tests on lithium iron phosphate batteries, extracting features such as sharp points and slopes from the voltage response curves. Utilizing the SVR method, they achieved an accurate estimation of battery SOH, with the final battery capacity estimation error being less than 1%. Beyond the basic SVR prediction model, Qin et al. [190] introduced a Particle Swarm Optimization (PSO) algorithm to optimize the parameters of the SVR, thereby enhancing the prediction accuracy of battery SOH. The SVR model is commonly used for regression tasks on small datasets. However, as the size of the training dataset increases, it directly leads to an increase in the number of support vectors, which in turn raises computational costs. Comparatively, the GPR is an emerging approach whose hyperparameters can be acquired adaptively and which is relatively easy to implement [191]. Furthermore, the GPR is built upon a probability-based form, which makes its prediction results highly interpretable [192].

On the other hand, the battery degradation process is a time-varying process. These dynamic characteristics have not been considered by the aforementioned methods. In contrast, deep learning models are more competitive in terms of feature-processing capabilities and data-fitting effects. Under this category, recurrent neural networks, especially the Long Short-Term Memory (LSTM) unit, have been effectively utilized to extract dynamic features through the information transition through memory cells. Qu et al. [193] introduced complete ensemble empirical mode decomposition with adaptive noise to denoise the battery health data, and then leveraged LSTM to construct a prediction model. By implementing a sliding window approach, an accurate estimation of battery SOH has been achieved. He et al. [194] proposed an LSTM algorithm based on a quantum genetic algorithm for battery SOH prediction. For the features extracted from raw data such as current and voltage, they employed random forest to screen out important features, which were then input into the LSTM network for SOH prediction. Fasahat et al. [195] put forward a hybrid model combining autoencoder and LSTM for battery capacity estimation. The data features extracted by AE were utilized to construct the hybrid LSTM prediction model.



Finally, the prediction errors of the constructed hybrid model were compared with those of conventional models such as LSTM, and the prediction results applied to the CACLE dataset validated the effectiveness of the hybrid model. Tang et al. further proposed a SOC estimation method that fused neural networks with the equivalent circuit model to capture the dynamic characteristics of a battery in a wide temperature range over the full SOC range [196]. Deep learning algorithms generally exhibit excellent self-learning and adaptability capabilities. However, as black box models, enhancing their interpretability and generalization performance remains an area that requires intensive research in the future.

The methods for battery SOH estimation are summarized in Figure 10. These methods can be categorized into three primary groups: experimental methods, model-driven approaches, and machine learning techniques. Notably, machine learning methods represent a fusion of experimental and model-based methodologies. Several comprehensive reviews have outlined these categories, highlighting their respective strengths and limitations [18,197,198].

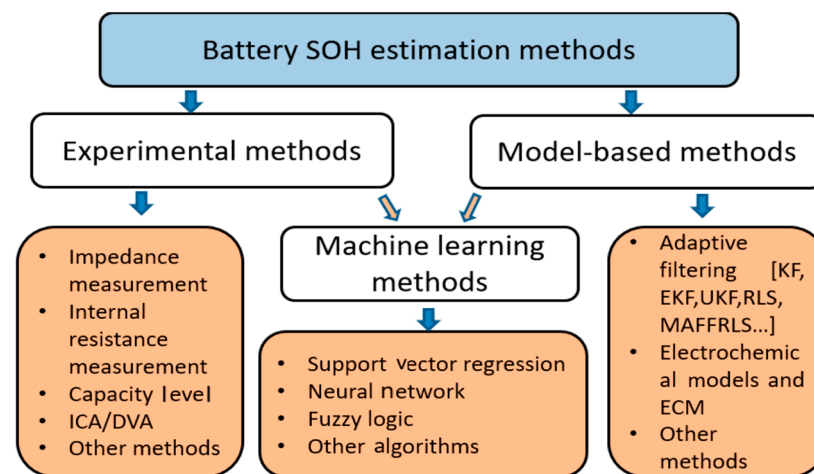


**Figure 10.** The method for battery SOH estimation [18].

### 3.5. The Software for Establishing and Running the Models

Employing appropriate software significantly enhances the efficiency of model establishment and execution. In this section, several popular software applications and their respective modeling capabilities are introduced:

Equivalent circuit models are typically established by Simulink, in which a highly intuitive visual interface allows users to create equivalent circuit models graphically. Various circuit element modules such as resistors, capacitors, inductors, and power sources can be set into the model by a simple drag-and-drop approach with a mouse. This graphical modeling method renders the process of constructing equivalent circuit models more intuitive and comprehensible, thereby lowering the threshold for modeling. Furthermore, a modular design is recommended in Simulink; a complex equivalent circuit model can be divided into multiple submodules for individual modeling and simulation. This modular approach not only enhances the scalability of the models but also facilitates collaboration and task division among team members.

Ready-made cases for the P2D model, SP model, and MP model can be found in COMSOL; on this basis, multiple physical fields can be coupled into the mechanistic models, thereby enabling a more accurate simulation of the working process of lithium-ion batteries. COMSOL's full coupling simulation capability allows researchers to comprehensively understand and analyze the complex mechanisms within the battery. However, due to the fact that some model assumptions and calculation methods are built-in within COMSOL, there are limitations to the flexibility in modifying the case models. Matlab is more powerful in terms of establishing custom models; Matlab offers a comprehensive set of toolboxes and function libraries that empower users to flexibly construct customized battery models.

Additionally, as a professional mathematical computing software, exceptional capabilities in numerical computation, symbolic computation, and graphics processing are included in Matlab. These strengths enable Matlab to efficiently handle the complex mathematical equations and algorithms involved in lithium-ion battery modeling. Furthermore, Matlab possesses robust data visualization functionalities, allowing users to intuitively present the simulation results of lithium-ion battery models in the form of charts, graphs, and curves. Sometimes, a synergy simulation of COMSOL and Matlab is required, in order to comprehensively utilize the advantages of Matlab in flexibility and COMSOL in multi-physics simulations.

Machine learning-based SOH estimation is commonly implemented through Python 3.7. As an open-source software, numerous publicly accessible packages for Python can be found in GitHub. And there are many libraries for data processing and machine learning, such as NumPy 1.20.3, Pandas 1.3.4, Scikit-learn 0.24.2, TensorFlow 2.8.0, PyTorch 1.13.1, and so on. These libraries offer extensive functionalities for data preprocessing, feature extraction, model training, and result evaluation, significantly simplifying the process of lithium-ion battery SOH estimation. SOH estimation for lithium batteries relies heavily on vast amounts of charging and discharging data, which typically encompass intricate parameters such as voltage, current, and temperature. The data processing libraries in Python can manage these data and extract features correlated with SOH efficiently. Additionally, multithreading, multiprocessing, and other parallel computing techniques are supported in Python, enabling further enhancements in data processing speed and efficiency.

#### 4. Challenges and Potential Directions for Future Research

Constructing mechanistic models for the cycling process of LIBs enables the efficient study of the relationship between electrode structure and battery performance, thereby assisting in the optimal design of electrode structures. Complemented by data-driven models, which can perform online estimation of the LIB health state based on battery operation data, the enhancement of LIB performance throughout its entire lifecycle can be achieved. However, as the design of electrode microstructures becomes increasingly intricate and sophisticated, and the requirements for the generalization capabilities of data-driven models are raised, there are still several problems that have not been effectively solved as yet. In this section, the current challenges of mechanistic and data-driven models are outlined, and potential directions for future research are proposed.

##### 4.1. Limitations of Mechanistic and Data-Driven Models

The operational mechanisms of LIBs include spatial multi-scale connections ranging from electrode microstructures to battery pack series-parallel configurations, as well as temporal cross-scale characteristics spanning molecular micro-motions to thousands of cycles of usage. This poses limitations on the coverage of the existing mechanistic models. In other words, spatial multi-scale models that consider electrode microstructures are often constrained by computational efficiency, making it difficult to simulate the evolution of battery health status over long-term usage. Conversely, temporal multi-scale models that account for gradual aging during battery cycling tend to significantly simplify spatial small-scale processes. One of the pressing issues is establishing a spatio-temporal multi-scale model that simultaneously considers electrode microstructures and the macro-performance of batteries over long-term operation. This would enable a more detailed investigation into the structure-performance relationship mechanisms of batteries. Model algorithm fusion and computational technology upgrades are effective means to achieve this goal. For instance, adopting suitable models to describe processes at different scales and then establishing multi-scale modeling through setting up information exchange between models. Additionally, attempts can be made to utilize parallel computing and GPU acceleration for the rapid computation of multi-scale models, thereby efficiently predicting state changes during long-term battery cycling processes.

Furthermore, mechanistic information is rarely incorporated into the online estimation of battery's actual operating states in the existing research. Currently, the mainstream data-driven models used for battery online monitoring lack internal mechanisms, making it difficult to extrapolate beyond the training data. While mechanistic models inherently excel in extrapolation compared to data-driven models, their disadvantages in computational efficiency often limit their application in online operation. Additionally, the internal mechanisms are deterministic in mechanistic models and cannot be adaptive, to consider the uncertain fluctuations arising from random factors during actual operation. The integrated development of mechanistic and data-driven models could represent a solution to overcome these current limitations, but another critical issue that needs to be addressed is how to comprehensively consider both the actual operating data and internal microscopic mechanisms within the model, and achieve accurate predictions of battery performance evolution over long periods based on early and limited data from the battery's operational process. Physics-Informed Neural Networks (PINNs) offer a specific model fusion paradigm; however, the consideration of mechanistic information in existing PINNs remains relatively simplistic, with mechanistic model components often limited to empirical models or equivalent circuit models. In the future, it is imperative to introduce mechanistic models that encompass more electrochemical information into neural network models.

#### 4.2. Future Prospects

To establish a long-term battery operation model that considers irregular electrode microstructures and spans across temporal scales, while maintaining a computational efficiency suitable for online operations, a promising approach is to decompose the reaction-diffusion processes within the electrode across various scales, including the diffusion processes within the solid-phase electrode, diffusion in the liquid-phase electrolyte, lithium-ion insertion/extraction reactions at the electrode surface, the growth of SEI layers, and lithium plating reactions. The portions involving irregular phase boundaries or moving interfaces can be described using CA, while those related to mass and energy conservation in physical fields can be modeled through PDEs. By leveraging the strengths of each modeling method for different processes, the efficient operation of individual model components can be achieved. Additionally, by establishing an information exchange between these models, a multi-scale model that considers the connection between electrode microstructures and macro-performance can be established.

On the other hand, image recognition techniques can be employed to process computed tomography images of specific electrodes, to obtain geometrical parameters and reconstruct two-dimensional morphologies of real electrodes, providing near-realistic solid-liquid phase boundary positions for the mechanistic model. Through model simulations, the evolution of unmeasurable variables such as concentration and potential within different electrode structures can be obtained, which enables the elucidation of the microscopic process mechanisms underlying the influence of electrode morphologies on battery performance, as well as the extraction of evolution patterns for key internal variables during long-term operation.

Moreover, to enhance the generalization performance of data-driven models in the real-time estimation of the battery health state, certain important pieces of mechanism information could be considered for integration. Hou et al. proposed a novel hybrid model that integrates both model-based and data-driven techniques for battery SOC estimation, in which an eXtreme Gradient Boosting model was adopted to further fit the residues from the battery model [199]. However, the integration of the mechanism model and the data-driven model is quite straightforward. Comparatively, an example of a PINN model is presented in Figure 11. By incorporating appropriate physical constraints, data-driven models can not only learn the distribution patterns within training data samples but also capture the physical laws described by mathematical equations. This integration imposes physical information constraints during the training process, enabling the model to develop a higher degree of generalization ability even with limited data samples. By incorporating such

constraints, the model learns not just from the data but also from the underlying physics, ultimately yielding a more robust and widely applicable solution.

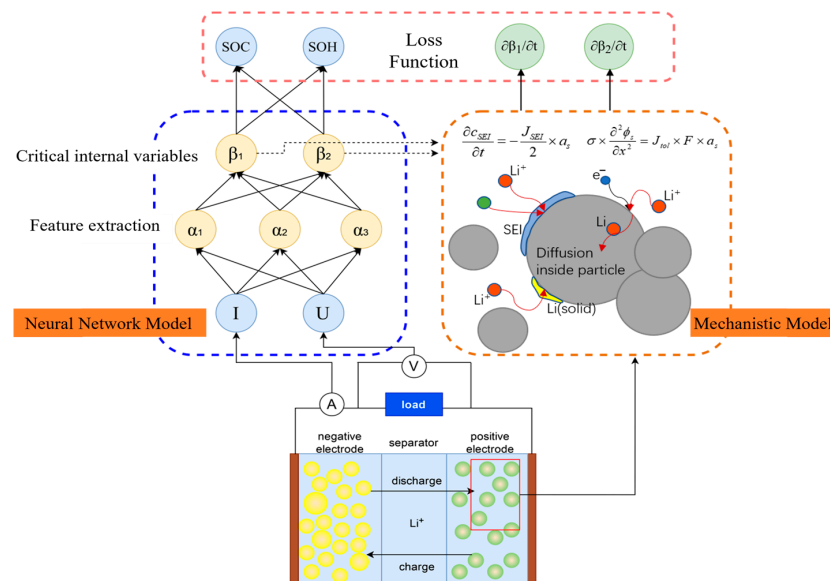


Figure 11. Schematic diagram of a PINN model for battery state estimation.

## 5. Conclusions

As a crucial technology driving energy transition and sustainable development, LIBs will occupy an increasingly important position in future energy systems. However, their current development is still hindered by issues such as battery safety, limited battery endurance, slow charging rates, and a short lifespan. Process mechanisms and operational data serve as two effective tools to assist in the optimal design of battery structures and the optimization of operational strategies. Investigating the internal operating mechanisms of LIBs and establishing mechanistic models that can correlate internal electrode states with macroscopic performance will enable the efficient optimization of electrode structures. Combining data-driven models to capture critical information from battery operational data and establishing machine learning models for the real-time prediction of battery health status hold significant research importance for enhancing the operational performance throughout the entire battery lifecycle. This work presents an overview of the existing mechanism-based and data-driven approaches to LIB modeling. The mechanistic models, including equivalent circuit models, electrochemical models, and CA models, are comprehensively reviewed. Considerations of electrode morphology and the battery aging mechanism, as well as their impact on battery performance in mechanistic models, are summarized. Then, data-driven models for the estimation of the battery health state in BMS are introduced from the perspectives of health indicator extraction, feature selection, and feature extraction. Finally, challenges and potential directions for future research are discussed. More efficient mechanistic modeling approaches and the integration of process mechanisms into data-driven models for the real-time estimation of battery health state are expected to be the future trend.

Based on this review, the future of LIBs is predicted to be developed in the following two directions. In terms of electrode structure design, this is a potential research direction to achieve intelligent electrode design by applying the mechanism model, so as to further improve charging efficiency, lifespan, and other battery performance metrics. The establishment of an electrochemical model that accurately describes the relationship between microscopic mechanisms and macroscopic properties can improve research efficiency by reducing the number of experiments. However, it is extremely difficult and unnecessary to build a mechanism model that connects microscopic and macroscopic information in sufficient detail. How to realize a multi-scale model that can guide experiments through model

simplification and numerical calculation methods is the challenge for the future. In terms of battery states estimation, a data–mechanism fusion modeling approach is a promising research direction. This can contribute to overcoming both the limitation of the extrapolative capabilities in data-driven models and the limitation of adaptability to random fluctuations in mechanism models. Essentially, through this fusion, the two approaches can compensate for each other's deficiencies. The PINN is one potential framework; however, existing PINNs do not systematically represent the internal process mechanisms of batteries. The challenge for the future lies in how to introduce more detailed mechanism information into data-driven models to achieve higher extrapolative capabilities and computation efficiency.

Given the limitations inherent in our literature review process, our analysis primarily reflects our current knowledge and understanding of this subject matter. Consequently, it is possible that not all relevant works in this field have been included, and we acknowledge the potential for misinterpretation of specific findings. Nevertheless, we aspire to have introduced a novel perspective on this topic and to offer a resource-rich reference point for our fellow researchers to build upon and from which to further explore.

**Author Contributions:** Conceptualization, W.S. and Y.T.; methodology, C.J. and J.D.; software, C.Z. and J.D.; validation, Y.T. and C.Z.; formal analysis, Y.T. and W.S.; investigation, C.J. and J.D.; resources, W.S.; data curation, C.J. and C.Z.; writing—original draft preparation, C.J. and J.D.; writing—review and editing, Y.T. and W.S.; visualization, C.J. and J.D.; supervision, J.W., W.S. and Y.T.; project administration, W.S. and Y.T.; funding acquisition, J.W. and W.S. All authors have read and agreed to the published version of the manuscript.

**Funding:** This research was funded by the National Natural Science Foundation of China, grant number 22278018.

**Data Availability Statement:** No new data were created or analyzed in this study.

**Conflicts of Interest:** The authors declare no conflicts of interest.

## Abbreviations

The description and units for the parameters and variables.

$c_s$	Lithium-Ion Concentration in Solid Phase	$\text{mol}\cdot\text{m}^{-3}$
$c_e$	Lithium-ion concentration in liquid phase	$\text{mol}\cdot\text{m}^{-3}$
$r$	Radial direction	m
$x$	Thickness direction	m
$t$	Time	s
$D_s$	Solid diffusion coefficient	$\text{m}^2\cdot\text{s}^{-1}$
$D_e$	Liquid diffusion coefficient	$\text{m}^2\cdot\text{s}^{-1}$
$t_0^+$	Transfer number	/
$J_{Li}$	Solid–liquid interfacial flux	$\text{mol}\cdot\text{m}^{-2}\cdot\text{s}^{-1}$
$\varepsilon_e$	Porosity	/
$F$	Faraday constant	$\text{C}\cdot\text{mol}^{-1}$
$\varphi_s$	Electric potential in solid phase	V
$\varphi_e$	Electric potential in liquid phase	V
$E_0$	Equilibrium potential	V
$\eta$	Reaction overpotential	V
$\sigma$	Conductivity of solid phase	$\text{S}\cdot\text{m}^{-1}$
$\kappa^{eff}$	Effective liquid-phase conductivity	$\text{S}\cdot\text{m}^{-1}$
$\kappa_d^{eff}$	Effective diffusion conductivity	$\text{A}\cdot\text{m}^{-1}$
$f$	Ionic activity coefficient	/
$T$	Temperature	K
$R$	Gas constant	$\text{J}\cdot\text{mol}^{-1}\cdot\text{K}^{-1}$
$c_{s,max}$	Maximum particle concentration	$\text{mol}\cdot\text{m}^{-3}$
$c_{s,surf}$	Particle surface concentration	$\text{mol}\cdot\text{m}^{-3}$
$c_s$	Lithium-ion concentration in solid phase	$\text{mol}\cdot\text{m}^{-3}$
$c_e$	Lithium-ion concentration in liquid phase	$\text{mol}\cdot\text{m}^{-3}$

## References

1. Omar, N.; Monem, M.A.; Firouz, Y.; Salminen, J.; Smekens, J.; Hegazy, O.; Gaulous, H.; Mulder, G.; Van den Bossche, P.; Coosemans, T.; et al. Lithium iron phosphate based battery—Assessment of the aging parameters and development of cycle life model. *Appl. Energy* **2014**, *113*, 1575–1585. [[CrossRef](#)]
2. Hu, X.; Wang, Z.; Zeng, S.; Guo, J.; Qin, T. Remaining capacity estimation of lithium-ion batteries based on the constant voltage charging profile. *PLoS ONE* **2018**, *13*, e0200169. [[CrossRef](#)]
3. Wang, Y.; Liu, B.; Li, Q.; Cartmell, S.; Ferrara, S.; Deng, Z.D.; Xiao, J. Lithium and lithium ion batteries for applications in microelectronic devices: A review. *J. Power Sources* **2015**, *286*, 330–345. [[CrossRef](#)]
4. Choi, S.; Wang, G. Advanced Lithium-Ion Batteries for Practical Applications: Technology, Development, and Future Perspectives. *Adv. Mater. Technol.* **2018**, *3*, 1700376. [[CrossRef](#)]
5. Li, Y.; Liu, K.L.; Foley, A.M.; Zülke, A.; Berecibar, M.; Nanini-Maury, E.; Van Mierlo, J.; Hoster, H.E. Data-driven health estimation and lifetime prediction of lithium-ion batteries: A review. *Renew. Sust. Energy Rev.* **2019**, *113*, 18. [[CrossRef](#)]
6. Masias, A.; Marcicki, J.; Paxton, W.A. Opportunities and Challenges of Lithium Ion Batteries in Automotive Applications. *ACS Energy Lett.* **2021**, *6*, 621–630. [[CrossRef](#)]
7. Tamilselvi, S.; Gunasundari, S.; Karuppiyah, N.; Rk, A.R.; Madhusudan, S.; Nagarajan, V.M.; Sathish, T.; Shamim, M.Z.M.; Saleel, C.A.; Afzal, A. A Review on Battery Modelling Techniques. *Sustainability* **2021**, *13*, 10042. [[CrossRef](#)]
8. Fotouhi, A.; Auger, D.J.; Propp, K.; Longo, S.; Wild, M. A review on electric vehicle battery modelling: From Lithium-ion toward Lithium–Sulphur. *Renew. Sustain. Energy Rev.* **2016**, *56*, 1008–1021. [[CrossRef](#)]
9. Abada, S.; Marlair, G.; Lecocq, A.; Petit, M.; Sauvart-Moynot, V.; Huët, F. Safety focused modeling of lithium-ion batteries: A review. *J. Power Sources* **2016**, *306*, 178–192. [[CrossRef](#)]
10. Meng, J.; Luo, G.; Ricco, M.; Swierczynski, M.; Stroe, D.-I.; Teodorescu, R. Overview of Lithium-Ion Battery Modeling Methods for State-of-Charge Estimation in Electrical Vehicles. *Appl. Sci.* **2018**, *8*, 659. [[CrossRef](#)]
11. Lucaferri, V.; Quercio, M.; Laudani, A.; Fulginei, F.R. A Review on Battery Model-Based and Data-Driven Methods for Battery Management Systems. *Energies* **2023**, *16*, 7807. [[CrossRef](#)]
12. Khaleghi, S.; Hosen, M.S.; Karimi, D.; Behi, H.; Beheshti, S.H.; Van Mierlo, J.; Berecibar, M. Developing an online data-driven approach for prognostics and health management of lithium-ion batteries. *Appl. Energy* **2022**, *308*, 118348. [[CrossRef](#)]
13. Chen, M.; Ma, G.; Liu, W.; Zeng, N.; Luo, X. An overview of data-driven battery health estimation technology for battery management system. *Neurocomputing* **2023**, *532*, 152–169. [[CrossRef](#)]
14. Hossain Lipu, M.S.; Hannan, M.A.; Karim, T.F.; Hussain, A.; Saad, M.H.M.; Ayob, A.; Miah, M.S.; Indra Mahlia, T.M. Intelligent algorithms and control strategies for battery management system in electric vehicles: Progress, challenges and future outlook. *J. Clean. Prod.* **2021**, *292*, 126044. [[CrossRef](#)]
15. Lin, Q.; Wang, J.; Xiong, R.; Shen, W.; He, H. Towards a smarter battery management system: A critical review on optimal charging methods of lithium ion batteries. *Energy* **2019**, *183*, 220–234. [[CrossRef](#)]
16. Ryan, E.M.; Mukherjee, P.P. Mesoscale modeling in electrochemical devices—A critical perspective. *Prog. Energy Combust. Sci.* **2019**, *71*, 118–142. [[CrossRef](#)]
17. How, D.N.T.; Hannan, M.A.; Lipu, M.S.H.; Ker, P.J. State of Charge Estimation for Lithium-Ion Batteries Using Model-Based and Data-Driven Methods: A Review. *IEEE Access* **2019**, *7*, 136116–136136. [[CrossRef](#)]
18. Wang, Z.; Feng, G.; Zhen, D.; Gu, F.; Ball, A. A review on online state of charge and state of health estimation for lithium-ion batteries in electric vehicles. *Energy Rep.* **2021**, *7*, 5141–5161. [[CrossRef](#)]
19. Ouyang, M.; Liu, G.; Lu, L.; Li, J.; Han, X. Enhancing the estimation accuracy in low state-of-charge area: A novel onboard battery model through surface state of charge determination. *J. Power Sources* **2014**, *270*, 221–237. [[CrossRef](#)]
20. Chen, X.; Shen, W.; Cao, Z.; Kapoor, A. A novel approach for state of charge estimation based on adaptive switching gain sliding mode observer in electric vehicles. *J. Power Sources* **2014**, *246*, 667–678. [[CrossRef](#)]
21. Galeotti, M.; Cinà, L.; Giammanco, C.; Cordiner, S.; Di Carlo, A. Performance analysis and SOH (state of health) evaluation of lithium polymer batteries through electrochemical impedance spectroscopy. *Energy* **2015**, *89*, 678–686. [[CrossRef](#)]
22. Zhu, J.; Knapp, M.; Darma, M.S.D.; Fang, Q.; Wang, X.; Dai, H.; Wei, X.; Ehrenberg, H. An improved electro-thermal battery model complemented by current dependent parameters for vehicular low temperature application. *Appl. Energy* **2019**, *248*, 149–161. [[CrossRef](#)]
23. Li, A.G.; Mayilvahanan, K.; West, A.C.; Preindl, M. Discrete-time modeling of Li-ion batteries with electrochemical overpotentials including diffusion. *J. Power Sources* **2021**, *500*, 229991. [[CrossRef](#)]
24. Li, S.E.; Wang, B.; Peng, H.; Hu, X. An electrochemistry-based impedance model for lithium-ion batteries. *J. Power Sources* **2014**, *258*, 9–18. [[CrossRef](#)]
25. Shrivastava, P.; Soon, T.K.; Idris, M.Y.I.B.; Mekhilef, S.; Adnan, S.B.R.S. Comprehensive co-estimation of lithium-ion battery state of charge, state of energy, state of power, maximum available capacity, and maximum available energy. *J. Energy Storage* **2022**, *56*, 106049. [[CrossRef](#)]
26. Tian, N.; Wang, Y.; Chen, J.; Fang, H. One-shot parameter identification of the Thevenin’s model for batteries: Methods and validation. *J. Energy Storage* **2020**, *29*, 101282. [[CrossRef](#)]
27. Guo, F.; Hu, G.; Xiang, S.; Zhou, P.; Hong, R.; Xiong, N. A multi-scale parameter adaptive method for state of charge and parameter estimation of lithium-ion batteries using dual Kalman filters. *Energy* **2019**, *178*, 79–88. [[CrossRef](#)]

28. Shrivastava, P.; Kok Soon, T.; Bin Idris, M.Y.I.; Mekhilef, S.; Adnan, S.B.R.S. Combined State of Charge and State of Energy Estimation of Lithium-Ion Battery Using Dual Forgetting Factor-Based Adaptive Extended Kalman Filter for Electric Vehicle Applications. *IEEE Trans. Veh. Technol.* **2021**, *70*, 1200–1215. [[CrossRef](#)]
29. Ozkurt, C.; Camci, F.; Atamuradov, V.; Odorrry, C. Integration of sampling based battery state of health estimation method in electric vehicles. *Appl. Energy* **2016**, *175*, 356–367. [[CrossRef](#)]
30. Liu, X.; Li, W.; Zhou, A. PNGV Equivalent Circuit Model and SOC Estimation Algorithm for Lithium Battery Pack Adopted in AGV Vehicle. *IEEE Access* **2018**, *6*, 23639–23647. [[CrossRef](#)]
31. Yan, X.W.; Guo, Y.W.; Cui, Y.; Wang, Y.W.; Deng, H.R. Electric Vehicle Battery SOC Estimation based on GNL Model Adaptive Kalman Filter. *J. Phys. Conf. Ser.* **2018**, *1087*, 052027. [[CrossRef](#)]
32. Peng, J.; Meng, J.; Wu, J.; Deng, Z.; Lin, M.; Mao, S.; Stroe, D.-I. A comprehensive overview and comparison of parameter benchmark methods for lithium-ion battery application. *J. Energy Storage* **2023**, *71*, 108197. [[CrossRef](#)]
33. Han, X.; Ouyang, M.; Lu, L.; Li, J. Simplification of physics-based electrochemical model for lithium ion battery on electric vehicle. Part I: Diffusion simplification and single particle model. *J. Power Sources* **2015**, *278*, 802–813. [[CrossRef](#)]
34. Han, X.; Ouyang, M.; Lu, L.; Li, J. Simplification of physics-based electrochemical model for lithium ion battery on electric vehicle. Part II: Pseudo-two-dimensional model simplification and state of charge estimation. *J. Power Sources* **2015**, *278*, 814–825. [[CrossRef](#)]
35. Liu, B.; Tang, X.; Gao, F. Joint estimation of battery state-of-charge and state-of-health based on a simplified pseudo-two-dimensional model. *Electrochim. Acta* **2020**, *344*, 136098. [[CrossRef](#)]
36. Kim, J.; Chun, H.; Baek, J.; Han, S. Parameter identification of lithium-ion battery pseudo-2-dimensional models using genetic algorithm and neural network cooperative optimization. *J. Energy Storage* **2022**, *45*, 103571. [[CrossRef](#)]
37. Kemper, P.; Li, S.E.; Kum, D. Simplification of pseudo two dimensional battery model using dynamic profile of lithium concentration. *J. Power Sources* **2015**, *286*, 510–525. [[CrossRef](#)]
38. Newman, J.; Tiedemann, W. Porous-electrode theory with battery applications. *AIChE J.* **1975**, *21*, 25–41. [[CrossRef](#)]
39. Fuller, T.F.; Doyle, M.; Newman, J. Simulation and Optimization of the Dual Lithium Ion Insertion Cell. *J. Electrochem. Soc.* **1994**, *141*, 1. [[CrossRef](#)]
40. Mu, W.; Liu, X.; Wen, Z.; Liu, L. Numerical simulation of the factors affecting the growth of lithium dendrites. *J. Energy Storage* **2019**, *26*, 100921. [[CrossRef](#)]
41. Jiang, Z.Y.; Qu, Z.G.; Zhou, L. Lattice Boltzmann simulation of ion and electron transport during the discharge process in a randomly reconstructed porous electrode of a lithium-ion battery. *Int. J. Heat Mass Transf.* **2018**, *123*, 500–513. [[CrossRef](#)]
42. Kespe, M.; Nirschl, H. Numerical simulation of lithium-ion battery performance considering electrode microstructure. *Int. J. Energy Res.* **2015**, *39*, 2062–2074. [[CrossRef](#)]
43. Lu, X.; Zhang, X.; Tan, C.; Heenan, T.M.M.; Lagnoni, M.; O'Regan, K.; Daemi, S.; Bertei, A.; Jones, H.G.; Hinds, G.; et al. Multi-length scale microstructural design of lithium-ion battery electrodes for improved discharge rate performance. *Energy Environ. Sci.* **2021**, *14*, 5929–5946. [[CrossRef](#)]
44. Li, J.; Wang, L.; Lyu, C.; Wang, H.; Liu, X. New method for parameter estimation of an electrochemical-thermal coupling model for LiCoO<sub>2</sub> battery. *J. Power Sources* **2016**, *307*, 220–230. [[CrossRef](#)]
45. Wu, W.; Xiao, X.; Huang, X.; Yan, S. A multiphysics model for the in situ stress analysis of the separator in a lithium-ion battery cell. *Comput. Mater. Sci.* **2014**, *83*, 127–136. [[CrossRef](#)]
46. Wang, Q.-K.; Shen, J.-N.; Ma, Z.-F.; He, Y.-J. Decoupling parameter estimation strategy based electrochemical-thermal coupled modeling method for large format lithium-ion batteries with internal temperature experimental validation. *Chem. Eng. J.* **2021**, *424*, 130308. [[CrossRef](#)]
47. Zhang, D.; Popov, B.N.; White, R.E. Modeling Lithium Intercalation of a Single Spinel Particle under Potentiodynamic Control. *J. Electrochem. Soc.* **2000**, *147*, 831. [[CrossRef](#)]
48. Santhanagopalan, S.; Guo, Q.; Ramadass, P.; White, R.E. Review of models for predicting the cycling performance of lithium ion batteries. *J. Power Sources* **2006**, *156*, 620–628. [[CrossRef](#)]
49. Tanim, T.R.; Rahn, C.D.; Wang, C.-Y. A Temperature Dependent, Single Particle, Lithium Ion Cell Model Including Electrolyte Diffusion. *J. Dyn. Syst. Meas. Control* **2015**, *137*, 011005. [[CrossRef](#)]
50. Guo, M.; Sikha, G.; White, R.E. Single-Particle Model for a Lithium-Ion Cell Thermal Behavior. *J. Electrochem. Soc.* **2011**, *158*, A122–A132. [[CrossRef](#)]
51. Safaria, M.; Delacourt, C. Mathematical Modeling of Lithium Iron Phosphate Electrode Galvanostatic Charge/Discharge and Path Dependence. *J. Electrochem. Soc.* **2011**, *158*, A63–A73. [[CrossRef](#)]
52. Farkhondeh, M.; Safari, M.; Pritzker, M.; Fowler, M.; Han, T.; Wang, J.; Delacourt, C. Full-Range Simulation of a Commercial LiFePO<sub>4</sub> Electrode Accounting for Bulk and Surface Effects: A Comparative Analysis. *J. Electrochem. Soc.* **2013**, *161*, A201–A212. [[CrossRef](#)]
53. Kim, G.-H.; Smith, K.; Lee, K.-J.; Santhanagopalan, S.; Pesaran, A. Multi-Domain Modeling of Lithium-Ion Batteries Encompassing Multi-Physics in Varied Length Scales. *J. Electrochem. Soc.* **2011**, *158*, A955. [[CrossRef](#)]
54. Allu, S.; Kalnaus, S.; Simunovic, S.; Nanda, J.; Turner, J.A.; Pannala, S. A three-dimensional meso-macroscopic model for Li-Ion intercalation batteries. *J. Power Sources* **2016**, *325*, 42–50. [[CrossRef](#)]
55. Lipnikov, K.; Manzini, G.; Shashkov, M. Mimetic finite difference method. *J. Comput. Phys.* **2014**, *257*, 1163–1227. [[CrossRef](#)]

56. Marinkovic, D.; Zehn, M. Survey of Finite Element Method-Based Real-Time Simulations. *Appl. Sci.* **2019**, *9*, 2775. [[CrossRef](#)]
57. Lim, Y.-I.; Chang, S.-C.; Jørgensen, S.B. A novel partial differential algebraic equation (PDAE) solver: Iterative space–time conservation element/solution element (CE/SE) method. *Comput. Chem. Eng.* **2004**, *28*, 1309–1324. [[CrossRef](#)]
58. Bizeray, A.M.; Zhao, S.; Duncan, S.R.; Howey, D.A. Lithium-ion battery thermal-electrochemical model-based state estimation using orthogonal collocation and a modified extended Kalman filter. *J. Power Sources* **2015**, *296*, 400–412. [[CrossRef](#)]
59. Kosch, S.; Zhao, Y.; Sturm, J.; Schuster, J.; Mulder, G.; Ayerbe, E.; Jossen, A. A Computationally Efficient Multi-Scale Model for Lithium-Ion Cells. *J. Electrochem. Soc.* **2018**, *165*, A2374–A2388. [[CrossRef](#)]
60. Kari, J. Theory of cellular automata: A survey. *Theor. Comput. Sci.* **2005**, *334*, 3–33. [[CrossRef](#)]
61. Packard, N.H.; Wolfram, S. Two-dimensional cellular automata. *J. Stat. Phys.* **1985**, *38*, 901–946. [[CrossRef](#)]
62. Xu, W.; Yan, G. A lattice Boltzmann model for the Navier-Stokes equation. *Microprocess. Microsyst.* **2023**, *96*, 104391. [[CrossRef](#)]
63. Chen, J.; Lyu, X.; Yu, Y.; Liu, B.; Liu, F.; Li, X.; Zhang, H.; Guo, Z. Improved cellular automata modeling of corrosion/oxidation mechanism of stainless steel in LBE. *Nucl. Eng. Des.* **2024**, *418*, 112876. [[CrossRef](#)]
64. Zheng, X.; Dai, W.; Shu, Z.; Zhao, D.; Liang, W.; Lei, G.; Qian, H. Numerical simulation of air solidification process in liquid hydrogen with LBM-CA coupled method. *Int. J. Hydrogen Energy* **2023**, *48*, 11567–11577. [[CrossRef](#)]
65. Ginota, V.; Souiss, C.L.P.S. A multi-agents architecture to enhance end-user individual-based modelling. *Ecol. Model.* **2002**, *157*, 23–41. [[CrossRef](#)]
66. Toffoli, T.; Capobianco, S.; Mentrasti, P. When—and how—can a cellular automaton be rewritten as a lattice gas? *Theor. Comput. Sci.* **2008**, *403*, 71–88. [[CrossRef](#)]
67. Patanarapeelert, K.; Frank, T.D.; Tang, I.M. From a cellular automaton model of tumor–immune interactions to its macroscopic dynamical equation: A drift–diffusion data analysis approach. *Math. Comput. Model.* **2011**, *53*, 122–130. [[CrossRef](#)]
68. Bandman, O.L. A cellular automata convection-diffusion model of flows through porous media. *Optoelectron. Instrum. Data Process.* **2007**, *43*, 524–529. [[CrossRef](#)]
69. Ai, J.; Zhai, C.; Du, H.; Dang, Y.; Dai, J.; Sun, W. Grid anisotropy of propagation fronts in cellular automata and its reduction methods. *Appl. Math. Comput.* **2024**, *482*, 128971. [[CrossRef](#)]
70. Gurikov, P.; Kolnoochenko, A.; Golubchikov, M.; Menshutina, N.; Smirnova, I. A synchronous cellular automaton model of mass transport in porous media. *Comput. Chem. Eng.* **2016**, *84*, 446–457. [[CrossRef](#)]
71. Ai, J.; Zhai, C.; Sun, W. Study on the Formation of Complex Chemical Waveforms by Different Computational Methods. *Processes* **2020**, *8*, 393. [[CrossRef](#)]
72. Ackland, G.J.; Tweedie, E.S. Microscopic model of diffusion limited aggregation and electrodeposition in the presence of leveling molecules. *Phys. Rev. E* **2006**, *73*, 011606. [[CrossRef](#)]
73. Pérez-Brokate, C.F.; di Caprio, D.; Mahé, É.; Féron, D.; de Lamare, J. Cyclic voltammetry simulations with cellular automata. *J. Comput. Sci.* **2015**, *11*, 269–278. [[CrossRef](#)]
74. Du, H.; Dai, J.; Ai, J.; Zhai, C.; Sun, W. A CA-LBM framework for simulating the lithium dendrite growth process. *J. Energy Storage* **2024**, *89*, 111702. [[CrossRef](#)]
75. Li, S.; Li, Z.; Xu, D.; Feng, G.; Hu, R. Porosity and tortuosity: Keys for accurate modeling of porous electrodes in supercapacitors. *Mater. Today Phys.* **2023**, *36*, 101174. [[CrossRef](#)]
76. Xie, W.; Guo, P.; Gao, X. Elucidating the rate limitation of lithium-ion batteries under different charging conditions through polarization analysis. *J. Energy Storage* **2024**, *82*, 110554. [[CrossRef](#)]
77. Zhao, D.; Chen, W. Analysis of polarization and thermal characteristics in lithium-ion battery with various electrode thicknesses. *J. Energy Storage* **2023**, *71*, 108159. [[CrossRef](#)]
78. Yu, J.; Duquesnoy, M.; Liu, C.; Franco, A.A. Optimization of the microstructure of carbon felt electrodes by applying the lattice Boltzmann method and Bayesian optimizer. *J. Power Sources* **2023**, *575*, 233182. [[CrossRef](#)]
79. Boyce, A.M.; Lu, X.; Brett, D.J.L.; Shearing, P.R. Exploring the influence of porosity and thickness on lithium-ion battery electrodes using an image-based model. *J. Power Sources* **2022**, *542*, 231779. [[CrossRef](#)]
80. Chen, Y.H.; Wang, C.W.; Zhang, X.; Sastry, A.M. Porous cathode optimization for lithium cells: Ionic and electronic conductivity, capacity, and selection of materials. *J. Power Sources* **2010**, *195*, 2851–2862. [[CrossRef](#)]
81. Zheng, H.; Liu, G.; Song, X.; Ridgway, P.; Xun, S.; Battaglia, V.S. Cathode Performance as a Function of Inactive Material and Void Fractions. *J. Electrochem. Soc.* **2010**, *157*, A1060–A1066. [[CrossRef](#)]
82. Zaghbi, K.; Song, X.; Guerfi, A.; Kostecki, R.; Kinoshita, K. Effect of particle morphology on lithium intercalation rates in natural graphite. *J. Power Sources* **2003**, *124*, 505–512. [[CrossRef](#)]
83. Lu, C.H.; Lin, S.W. Influence of the particle size on the electrochemical properties of lithium manganese oxide. *J. Power Sources* **2001**, *97*, 458–460. [[CrossRef](#)]
84. Sivakkumar, S.R.; Nerkar, J.Y.; Pandolfo, A.G. Rate capability of graphite materials as negative electrodes in lithium-ion capacitors. *Electrochim. Acta* **2010**, *55*, 3330–3335. [[CrossRef](#)]
85. Frankenberger, M.; Singh, M.; Dinter, A.; Jankowsky, S.; Schmidt, A.; Pettinger, K.-H. Laminated Lithium Ion Batteries with improved fast charging capability. *J. Electroanal. Chem.* **2019**, *837*, 151–158. [[CrossRef](#)]
86. Kalnaus, S.; Livingston, K.; Hawley, W.B.; Wang, H.; Li, J. Design and processing for high performance Li ion battery electrodes with double-layer structure. *J. Energy Storage* **2021**, *44*, 103582. [[CrossRef](#)]



87. Methekar, R.N.; Boovaragavan, V.; Arabandi, M.; Ramadesigan, V.; Subramanian, V.R.; Latinwo, F.; Braatz, R.D. Optimal spatial distribution of microstructure in porous electrodes for Li-ion batteries. In Proceedings of the 2010 American Control Conference, Baltimore, MD, USA, 30 June–2 July 2010.
88. Qi, Y.; Jang, T.; Ramadesigan, V.; Schwartz, D.T.; Subramanian, V.R. Is There a Benefit in Employing Graded Electrodes for Lithium-Ion Batteries? *J. Electrochem. Soc.* **2017**, *164*, A3196–A3207. [[CrossRef](#)]
89. Golmon, S.; Maute, K.; Dunn, M.L. A design optimization methodology for Li+ batteries. *J. Power Sources* **2014**, *253*, 239–250. [[CrossRef](#)]
90. Dai, Y.; Srinivasan, V. On Graded Electrode Porosity as a Design Tool for Improving the Energy Density of Batteries. *J. Electrochem. Soc.* **2015**, *163*, A406–A416. [[CrossRef](#)]
91. Bläubaum, L.; Röder, F.; Nowak, C.; Chan, H.S.; Kwade, A.; Krewer, U. Impact of Particle Size Distribution on Performance of Lithium-Ion Batteries. *ChemElectroChem* **2020**, *7*, 4755–4766. [[CrossRef](#)]
92. Taleghani, S.T.; Marcos, B.; Zaghbi, K.; Lantagne, G. A Study on the Effect of Porosity and Particles Size Distribution on Li-Ion Battery Performance. *J. Electrochem. Soc.* **2017**, *164*, E3179–E3189. [[CrossRef](#)]
93. Kanchan, B.K.; Randive, P. Investigation on capacity extension through non-uniform anode microstructure in lithium-ion battery. *Int. J. Heat Mass Transf.* **2023**, *214*, 124413. [[CrossRef](#)]
94. Zhu, P.; Slater, P.R.; Kendrick, E. Insights into architecture, design and manufacture of electrodes for lithium-ion batteries. *Mater. Des.* **2022**, *223*, 111208. [[CrossRef](#)]
95. Wang, Z.; Dai, C.; Chen, K.; Wang, Y.; Liu, Q.; Liu, Y.; Ma, B.; Mi, L.; Mao, W. Perspectives on strategies and techniques for building robust thick electrodes for lithium-ion batteries. *J. Power Sources* **2022**, *551*, 232176. [[CrossRef](#)]
96. Röder, F.; Sonntag, S.; Schröder, D.; Krewer, U. Simulating the Impact of Particle Size Distribution on the Performance of Graphite Electrodes in Lithium-Ion Batteries. *Energy Technol.* **2016**, *4*, 1588–1597. [[CrossRef](#)]
97. Kirk, T.L.; Evans, J.; Please, C.P.; Chapman, S.J. Modeling electrode heterogeneity in lithium-ion batteries unimodal and bimodal particle-size distributions. *SIAM J. Appl. Math.* **2022**, *82*, 625–653. [[CrossRef](#)]
98. Sharma, A.R.; Sai, C.S.; Kumar, A.; Jayasimha Reddy, R.V.; Danyharsha, D.; Jilte, R. Three-dimensional CFD study on heat dissipation in cylindrical lithium-ion battery module. *Mater. Today Proc.* **2021**, *46*, 10964–10968. [[CrossRef](#)]
99. Dai, J.; Zhai, C.; Lv, H.; Dang, Y.; Yu, G.; Sun, W.; Liu, Y. Electrode microstructure design based on a CA-FD hybrid computation framework to alleviate the concentration polarization. *J. Energy Storage* **2024**, *79*, 110142. [[CrossRef](#)]
100. Jokar, A.; Rajabloo, B.; Désilets, M.; Lacroix, M. Review of simplified Pseudo-two-Dimensional models of lithium-ion batteries. *J. Power Sources* **2016**, *327*, 44–55. [[CrossRef](#)]
101. Zhou, H.; Gao, L.T.; Li, Y.; Lyu, Y.; Guo, Z.-S. Electrochemical performance of lithium-ion batteries with two-layer gradient electrode architectures. *Electrochim. Acta* **2024**, *476*, 143656. [[CrossRef](#)]
102. Gao, Y.; Zhu, J.; Zhang, X. Evaluation of the Effect of Multiparticle on Lithium-Ion Battery Performance Using an Electrochemical Model. *IEEE/CAA J. Autom. Sin.* **2022**, *9*, 1896–1898. [[CrossRef](#)]
103. Dai, J.; Zhai, C.; Ai, J.; Yu, G.; Lv, H.; Sun, W.; Liu, Y. A cellular automata framework for porous electrode reconstruction and reaction-diffusion simulation. *Chin. J. Chem. Eng.* **2023**, *60*, 262–274. [[CrossRef](#)]
104. Vennam, G.; Sahoo, A.; Ahmed, S. A survey on lithium-ion battery internal and external degradation modeling and state of health estimation. *J. Energy Storage* **2022**, *52*, 17. [[CrossRef](#)]
105. Attia, P.M.; Bills, A.; Brosa Planella, F.; Dechent, P.; dos Reis, G.; Dubarry, M.; Gasper, P.; Gilchrist, R.; Greenbank, S.; Howey, D.; et al. Review—“Knees” in Lithium-Ion Battery Aging Trajectories. *J. Electrochem. Soc.* **2022**, *169*, 060517. [[CrossRef](#)]
106. Spotnitz, R. Simulation of capacity fade in lithium-ion batteries. *J. Power Sources* **2003**, *113*, 72–80. [[CrossRef](#)]
107. Liu, L.; Park, J.; Lin, X.; Sastry, A.M.; Lu, W. A thermal-electrochemical model that gives spatial-dependent growth of solid electrolyte interphase in a Li-ion battery. *J. Power Sources* **2014**, *268*, 482–490. [[CrossRef](#)]
108. Guan, P.; Liu, L.; Lin, X. Simulation and Experiment on Solid Electrolyte Interphase (SEI) Morphology Evolution and Lithium-Ion Diffusion. *J. Electrochem. Soc.* **2015**, *162*, A1798–A1808. [[CrossRef](#)]
109. Xie, Y.; Li, J.; Yuan, C. Multiphysics modeling of lithium ion battery capacity fading process with solid-electrolyte interphase growth by elementary reaction kinetics. *J. Power Sources* **2014**, *248*, 172–179. [[CrossRef](#)]
110. Kim, S.-P.; Duin, A.C.T.V.; Shenoy, V.B. Effect of electrolytes on the structure and evolution of the solid electrolyte interphase (SEI) in Li-ion batteries: A molecular dynamics study. *J. Power Sources* **2011**, *196*, 8590–8597. [[CrossRef](#)]
111. Ramadass, P.; Haran, B.; Gomadam, P.M.; White, R.; Popov, B.N. Development of First Principles Capacity Fade Model for Li-Ion Cells. *J. Electrochem. Soc.* **2004**, *151*, A196–A203. [[CrossRef](#)]
112. Prada, E.; Di Domenico, D.; Creff, Y.; Bernard, J.; Sauvant-Moynot, V.; Huet, F. A Simplified Electrochemical and Thermal Aging Model of LiFePO<sub>4</sub>-Graphite Li-ion Batteries: Power and Capacity Fade Simulations. *J. Electrochem. Soc.* **2013**, *160*, A616–A628. [[CrossRef](#)]
113. Tan, L.; Zhang, L.; Sun, Q.; Shen, M.; Qu, Q.; Zheng, H. Capacity loss induced by lithium deposition at graphite anode for LiFePO<sub>4</sub>/graphite cell cycling at different temperatures. *Electrochim. Acta* **2013**, *111*, 802–808. [[CrossRef](#)]
114. Sungjemmenla, S.K.V.; Soni, C.B.; Kumar, V.; Seh, Z.W. Understanding the Cathode–Electrolyte Interphase in Lithium-Ion Batteries. *Energy Technol.* **2022**, *10*, 2200421. [[CrossRef](#)]
115. Schuster, S.F.; Bach, T.; Fleder, E.; Müller, J.; Brand, M.; SEXTL, G.; Jossen, A. Nonlinear aging characteristics of lithium-ion cells under different operational conditions. *J. Energy Storage* **2015**, *1*, 44–53. [[CrossRef](#)]

116. Klett, M.; Svens, P.; Tengstedt, C.; Seyeux, A.; Światowska, J.; Lindbergh, G.; Wreland Lindström, R. Uneven Film Formation across Depth of Porous Graphite Electrodes in Cycled Commercial Li-Ion Batteries. *J. Phys. Chem. C* **2014**, *119*, 90–100. [[CrossRef](#)]
117. Broussely, M.; Biensan, P.; Bonhomme, F.; Blanchard, P.; Herreyre, S.; Nechev, K.; Staniewicz, R.J. Main aging mechanisms in Li ion batteries. *J. Power Sources* **2005**, *146*, 90–96. [[CrossRef](#)]
118. Legrand, N.; Knosp, B.; Desprez, P.; Lapticque, F.; Raël, S. Physical characterization of the charging process of a Li-ion battery and prediction of Li plating by electrochemical modelling. *J. Power Sources* **2014**, *245*, 208–216. [[CrossRef](#)]
119. Uhlmann, C.; Illig, J.; Ender, M.; Schuster, R.; Ivers-Tiffée, E. In situ detection of lithium metal plating on graphite in experimental cells. *J. Power Sources* **2015**, *279*, 428–438. [[CrossRef](#)]
120. Klett, M.; Eriksson, R.; Groot, J.; Svens, P.; Ciosek Högström, K.; Lindström, R.W.; Berg, H.; Gustafson, T.; Lindbergh, G.; Edström, K. Non-uniform aging of cycled commercial LiFePO<sub>4</sub>/graphite cylindrical cells revealed by post-mortem analysis. *J. Power Sources* **2014**, *257*, 126–137. [[CrossRef](#)]
121. Waldmann, T.; Hogg, B.-I.; Wohlfahrt-Mehrens, M. Li plating as unwanted side reaction in commercial Li-ion cells—A review. *J. Power Sources* **2018**, *384*, 107–124. [[CrossRef](#)]
122. Ge, H.; Aoki, T.; Ikeda, N.; Suga, S.; Isobe, T.; Li, Z.; Tabuchi, Y.; Zhang, J. Investigating Lithium Plating in Lithium-Ion Batteries at Low Temperatures Using Electrochemical Model with NMR Assisted Parameterization. *J. Electrochem. Soc.* **2017**, *164*, A1050–A1060. [[CrossRef](#)]
123. Arora, P.; Doyle, M.; White, R.E. Mathematical Modeling of the Lithium Deposition Overcharge Reaction in Lithium-Ion Batteries Using Carbon-Based Negative Electrodes. *J. Electrochem. Soc.* **1999**, *146*, 3543–3553. [[CrossRef](#)]
124. Yang, X.-G.; Leng, Y.; Zhang, G.; Ge, S.; Wang, C.-Y. Modeling of lithium plating induced aging of lithium-ion batteries: Transition from linear to nonlinear aging. *J. Power Sources* **2017**, *360*, 28–40. [[CrossRef](#)]
125. Aurbach, D.; Markovsky, B.; Rodkin, A.; Levi, E.; Cohen, Y.S.; Kim, H.J.; Schmidt, M. On the capacity fading of LiCoO<sub>2</sub> intercalation electrodes the effect of cycling, storage, temperature, and surface film forming additives. *Electrochim. Acta* **2002**, *47*, 4291–4306. [[CrossRef](#)]
126. Wu, N.; Yang, D.; Liu, J.; Tian, W. Study on accelerated capacity fade of LiMn<sub>2</sub>O<sub>4</sub>/graphite batteries under operating-mode cycling conditions. *Electrochim. Acta* **2012**, *62*, 91–96. [[CrossRef](#)]
127. Fang, X.; Ding, N.; Feng, X.Y.; Lu, Y.; Chen, C.H. Study of LiNi<sub>0.5</sub>Mn<sub>1.5</sub>O<sub>4</sub> synthesized via a chloride-ammonia co-precipitation method: Electrochemical performance, diffusion coefficient and capacity loss mechanism. *Electrochim. Acta* **2009**, *54*, 7471–7475. [[CrossRef](#)]
128. Yoon, T.; Nguyen, C.C.; Seo, D.M.; Lucht, B.L. Capacity Fading Mechanisms of Silicon Nanoparticle Negative Electrodes for Lithium Ion Batteries. *J. Electrochem. Soc.* **2015**, *162*, A2325–A2330. [[CrossRef](#)]
129. Markevich, E.; Sharabi, R.; Gottlieb, H.; Borgel, V.; Fridman, K.; Salitra, G.; Aurbach, D.; Semrau, G.; Schmidt, M.A.; Schall, N.; et al. Reasons for capacity fading of LiCoPO<sub>4</sub> cathodes in LiPF<sub>6</sub> containing electrolyte solutions. *Electrochem. Commun.* **2012**, *15*, 22–25. [[CrossRef](#)]
130. Wu, B.; Mu, Y.; Li, Z.; Li, M.; Zeng, L.; Zhao, T. Realizing high-voltage aqueous zinc-ion batteries with expanded electrolyte electrochemical stability window. *Chin. Chem. Lett.* **2023**, *34*, 107629. [[CrossRef](#)]
131. Klass, V.; Behm, M.; Lindbergh, G. A support vector machine-based state-of-health estimation method for lithium-ion batteries under electric vehicle operation. *J. Power Sources* **2014**, *270*, 262–272. [[CrossRef](#)]
132. Ji, S.L.; Zhu, J.X.; Yang, Y.X.; dos Reis, G.; Zhang, Z.S. Data-Driven Battery Characterization and Prognosis: Recent Progress, Challenges, and Prospects. *Small Methods* **2024**, *17*, 2301021. [[CrossRef](#)] [[PubMed](#)]
133. Lipu, M.S.H.; Hannan, M.A.; Hussain, A.; Ayob, A.; Saad, M.H.M.; Karim, T.F.; How, D.N.T. Data-driven state of charge estimation of lithium-ion batteries: Algorithms, implementation factors, limitations and future trends. *J. Clean. Prod.* **2020**, *277*, 29. [[CrossRef](#)]
134. Eleftheriadis, P.; Giazitzis, S.; Leva, S.; Ogliari, E. Data-Driven Methods for the State of Charge Estimation of Lithium-Ion Batteries: An Overview. *Forecasting* **2023**, *5*, 576–599. [[CrossRef](#)]
135. Wang, Y.J.; Tian, J.Q.; Sun, Z.D.; Wang, L.; Xu, R.L.; Li, M.C.; Chen, Z.H. A comprehensive review of battery modeling and state estimation approaches for advanced battery management systems. *Renew. Sust. Energy Rev.* **2020**, *131*, 18. [[CrossRef](#)]
136. Lin, C.; Tang, A.; Wang, W. A Review of SOH Estimation Methods in Lithium-ion Batteries for Electric Vehicle Applications. *Energy Procedia* **2015**, *75*, 1920–1925. [[CrossRef](#)]
137. Wu, L.F.; Fu, X.H.; Guan, Y. Review of the Remaining Useful Life Prognostics of Vehicle Lithium-Ion Batteries Using Data-Driven Methodologies. *Appl. Sci.* **2016**, *6*, 166. [[CrossRef](#)]
138. Barrow, D.K. Forecasting intraday call arrivals using the seasonal moving average method. *J. Bus. Res.* **2016**, *69*, 6088–6096. [[CrossRef](#)]
139. Zhao, Y.; Wang, S.; Xiao, F. A statistical fault detection and diagnosis method for centrifugal chillers based on exponentially-weighted moving average control charts and support vector regression. *Appl. Therm. Eng.* **2013**, *51*, 560–572. [[CrossRef](#)]
140. Sangiri, J.B.; Kulshreshtha, T.; Ghosh, S.; Maiti, S.; Chakraborty, C. A novel methodology to estimate the state-of-health and remaining-useful-life of a Li-ion battery using discrete Fourier transformation. *J. Energy Storage* **2022**, *46*, 103849. [[CrossRef](#)]
141. Fu, Y.; Xu, J.; Shi, M.; Mei, X. A Fast Impedance Calculation-Based Battery State-of-Health Estimation Method. *IEEE Trans. Ind. Electron.* **2022**, *69*, 7019–7028. [[CrossRef](#)]
142. Cheng, Y.; Zhang, X.; Wang, X.; Li, J. Battery State of Charge Estimation Based on Composite Multiscale Wavelet Transform. *Energies* **2022**, *15*, 2064. [[CrossRef](#)]

143. Cheng, G.; Wang, X.; He, Y. Remaining useful life and state of health prediction for lithium batteries based on empirical mode decomposition and a long and short memory neural network. *Energy* **2021**, *232*, 121022. [[CrossRef](#)]
144. Geslin, A.; van Vlijmen, B.; Cui, X.; Bhargava, A.; Asinger, P.A.; Braatz, R.D.; Chueh, W.C. Selecting the appropriate features in battery lifetime predictions. *Joule* **2023**, *7*, 1956–1965. [[CrossRef](#)]
145. Guo, Y.; Huang, K.; Yu, X.; Wang, Y. State-of-health estimation for lithium-ion batteries based on historical dependency of charging data and ensemble SVR. *Electrochim. Acta* **2022**, *428*, 140940. [[CrossRef](#)]
146. Liu, G.; Zhang, X.; Liu, Z. State of health estimation of power batteries based on multi-feature fusion models using stacking algorithm. *Energy* **2022**, *259*, 124851. [[CrossRef](#)]
147. Pang, X.X.; Zhong, S.; Wang, Y.L.; Yang, W.; Zheng, W.Z.; Sun, G.Z. A Review on the Prediction of Health State and Serving Life of Lithium-Ion Batteries. *Chem. Rec.* **2022**, *22*, 21. [[CrossRef](#)]
148. Luo, K.; Chen, X.; Zheng, H.R.; Shi, Z.C. A review of deep learning approach to predicting the state of health and state of charge of lithium-ion batteries. *J. Energy Chem.* **2022**, *74*, 159–173. [[CrossRef](#)]
149. Topan, P.A.; Ramadan, M.N.; Fathoni, G.; Cahyadi, A.I.; Wahyunggoro, O. State of Charge (SOC) and State of Health (SOH) estimation on lithium polymer battery via Kalman filter. In Proceedings of the 2016 2nd International Conference on Science and Technology-Computer (ICST), Yogyakarta, Indonesia, 27–28 October 2016; pp. 93–96.
150. Sepasi, S.; Ghorbani, R.; Liaw, B.Y. Inline state of health estimation of lithium-ion batteries using state of charge calculation. *J. Power Sources* **2015**, *299*, 246–254. [[CrossRef](#)]
151. Ren, Z.; Du, C.Q. A review of machine learning state-of-charge and state-of-health estimation algorithms for lithium-ion batteries. *Energy Rep.* **2023**, *9*, 2993–3021. [[CrossRef](#)]
152. Qi, N.; Yan, K.; Yu, Y.J.; Li, R.; Huang, R.; Chen, L.; Su, Y.F. Machine learning and neural network supported state of health simulation and forecasting model for lithium-ion battery. *Front. Energy* **2024**, *18*, 223–240. [[CrossRef](#)]
153. Li, X.J.; Yu, D.; Byg, V.S.; Ioan, S.D. The development of machine learning-based remaining useful life prediction for lithium-ion batteries. *J. Energy Chem.* **2023**, *82*, 103–121. [[CrossRef](#)]
154. Sharma, P.; Bora, B.J. A Review of Modern Machine Learning Techniques in the Prediction of Remaining Useful Life of Lithium-Ion Batteries. *Batteries* **2023**, *9*, 13. [[CrossRef](#)]
155. Madani, S.S.; Ziebert, C.; Vahdatkhal, P.; Sadrnezhaad, S.K. Recent Progress of Deep Learning Methods for Health Monitoring of Lithium-Ion Batteries. *Batteries* **2024**, *10*, 204. [[CrossRef](#)]
156. Samanta, A.; Chowdhuri, S.; Williamson, S.S. Machine Learning-Based Data-Driven Fault Detection/Diagnosis of Lithium-Ion Battery: A Critical Review. *Electronics* **2021**, *10*, 1309. [[CrossRef](#)]
157. Kim, E.; Kim, M.; Kim, J.; Kim, J.; Park, J.H.; Kim, K.T.; Park, J.H.; Kim, T.; Min, K.Y.M. Data-Driven Methods for Predicting the State of Health, State of Charge, and Remaining Useful Life of Li-Ion Batteries: A Comprehensive Review. *Int. J. Precis. Eng. Manuf.* **2023**, *24*, 1281–1304. [[CrossRef](#)]
158. Severson, K.A.; Attia, P.M.; Jin, N.; Perkins, N.; Jiang, B.; Yang, Z.; Chen, M.H.; Aykol, M.; Herring, P.K.; Fraggadakis, D.; et al. Data-driven prediction of battery cycle life before capacity degradation. *Nat. Energy* **2019**, *4*, 383–391. [[CrossRef](#)]
159. Tao, T.; Ji, C.; Dai, J.; Rao, J.; Wang, J.; Sun, W.; Romagnoli, J. Data-based health indicator extraction for battery SOH estimation via deep learning. *J. Energy Storage* **2024**, *78*, 109982. [[CrossRef](#)]
160. Zhang, Y.; Tang, Q.; Zhang, Y.; Wang, J.; Stimming, U.; Lee, A.A. Identifying degradation patterns of lithium ion batteries from impedance spectroscopy using machine learning. *Nat. Commun.* **2020**, *11*, 1706. [[CrossRef](#)]
161. Barkholtz, H.M.; Fresquez, A.; Chalamala, B.R.; Ferreira, S.R. A Database for Comparative Electrochemical Performance of Commercial 18650-Format Lithium-Ion Cells. *J. Electrochem. Soc.* **2017**, *164*, A2697–A2706. [[CrossRef](#)]
162. Ma, G.; Xu, S.; Jiang, B.; Cheng, C.; Yang, X.; Shen, Y.; Yang, T.; Huang, Y.; Ding, H.; Yuan, Y. Real-time personalized health status prediction of lithium-ion batteries using deep transfer learning. *Energy Environ. Sci.* **2022**, *15*, 4083–4094. [[CrossRef](#)]
163. Li, Y.; Stroe, D.-I.; Cheng, Y.; Sheng, H.; Sui, X.; Teodorescu, R. On the feature selection for battery state of health estimation based on charging–discharging profiles. *J. Energy Storage* **2021**, *33*, 102122. [[CrossRef](#)]
164. Xiong, W.; Mo, Y.; Yan, C. Online State-of-Health Estimation for Second-Use Lithium-Ion Batteries Based on Weighted Least Squares Support Vector Machine. *IEEE Access* **2021**, *9*, 1870–1881. [[CrossRef](#)]
165. Chen, J.; Marlow, M.N.; Jiang, Q.; Wu, B. Peak-tracking method to quantify degradation modes in lithium-ion batteries via differential voltage and incremental capacity. *J. Energy Storage* **2022**, *45*, 103669. [[CrossRef](#)]
166. Zheng, L.; Zhu, J.; Lu, D.D.-C.; Wang, G.; He, T. Incremental capacity analysis and differential voltage analysis based state of charge and capacity estimation for lithium-ion batteries. *Energy* **2018**, *150*, 759–769. [[CrossRef](#)]
167. Fly, A.; Chen, R. Rate dependency of incremental capacity analysis (dQ/dV) as a diagnostic tool for lithium-ion batteries. *J. Energy Storage* **2020**, *29*, 101329. [[CrossRef](#)]
168. Li, Y.; Zou, C.; Berecibar, M.; Nanini-Maury, E.; Chan, J.C.W.; van den Bossche, P.; Van Mierlo, J.; Omar, N. Random forest regression for online capacity estimation of lithium-ion batteries. *Appl. Energy* **2018**, *232*, 197–210. [[CrossRef](#)]
169. Ospina Agudelo, B.; Zamboni, W.; Monmasson, E. Application domain extension of incremental capacity-based battery SoH indicators. *Energy* **2021**, *234*, 121224. [[CrossRef](#)]

170. Tang, X.; Wang, Y.; Liu, Q.; Gao, F. Reconstruction of the incremental capacity trajectories from current-varying profiles for lithium-ion batteries. *iScience* **2021**, *24*, 103103. [[CrossRef](#)] [[PubMed](#)]
171. Weng, C.; Cui, Y.; Sun, J.; Peng, H. On-board state of health monitoring of lithium-ion batteries using incremental capacity analysis with support vector regression. *J. Power Sources* **2013**, *235*, 36–44. [[CrossRef](#)]
172. Wen, J.; Chen, X.; Li, X.; Li, Y. SOH prediction of lithium battery based on IC curve feature and BP neural network. *Energy* **2022**, *261*, 125234. [[CrossRef](#)]
173. Goh, H.H.; Lan, Z.; Zhang, D.; Dai, W.; Kurniawan, T.A.; Goh, K.C. Estimation of the state of health (SOH) of batteries using discrete curvature feature extraction. *J. Energy Storage* **2022**, *50*, 104646. [[CrossRef](#)]
174. Hu, X.; Che, Y.; Lin, X.; Onori, S. Battery Health Prediction Using Fusion-Based Feature Selection and Machine Learning. *IEEE Trans. Transp. Electrification* **2021**, *7*, 382–398. [[CrossRef](#)]
175. Khalid, S.; Khalil, T.; Nasreen, S. A survey of feature selection and feature extraction techniques in machine learning. In Proceedings of the 2014 Science and Information Conference, London, UK, 9 October 2014.
176. Saeys, Y.; Inza, I.; Larrañaga, P. A review of feature selection techniques in bioinformatics. *Bioinformatics* **2007**, *23*, 2507–2517. [[CrossRef](#)] [[PubMed](#)]
177. Vergara, J.R.; Estévez, P.A. A review of feature selection methods based on mutual information. *Neural Comput. Appl.* **2013**, *24*, 175–186. [[CrossRef](#)]
178. Ji, C.; Ma, F.; Wang, J.; Sun, W. Profitability related industrial-scale batch processes monitoring via deep learning based soft sensor development. *Comput. Chem. Eng.* **2023**, *170*, 108125. [[CrossRef](#)]
179. Estevez, P.A.; Tesmer, M.; Perez, C.A.; Zurada, J.M. Normalized Mutual Information Feature Selection. *IEEE Trans. Neural Netw.* **2009**, *20*, 189–201. [[CrossRef](#)]
180. Reshef, D.N.; Reshef, Y.A.; Finucane, H.K.; Grossman, S.R.; McVean, G.; Turnbaugh, P.J.; Lander, E.S.; Mitzenmacher, M.; Sabeti, P.C. Detecting Novel Associations in Large Data Sets. *Science* **2011**, *334*, 1518–1524. [[CrossRef](#)]
181. Freeman, C.; Kulić, D.; Basir, O. An evaluation of classifier-specific filter measure performance for feature selection. *Pattern Recognit.* **2015**, *48*, 1812–1826. [[CrossRef](#)]
182. Bennasar, M.; Hicks, Y.; Setchi, R. Feature selection using Joint Mutual Information Maximisation. *Expert Syst. Appl.* **2015**, *42*, 8520–8532. [[CrossRef](#)]
183. Xiao, L.; Wang, C.; Dong, Y.; Wang, J. A novel sub-models selection algorithm based on max-relevance and min-redundancy neighborhood mutual information. *Inf. Sci.* **2019**, *486*, 310–339. [[CrossRef](#)]
184. Yin, K.; Zhai, J.; Xie, A.; Zhu, J. Feature selection using max dynamic relevancy and min redundancy. *Pattern Anal. Appl.* **2023**, *26*, 631–643. [[CrossRef](#)]
185. Che, J.; Yang, Y.; Li, L.; Bai, X.; Zhang, S.; Deng, C. Maximum relevance minimum common redundancy feature selection for nonlinear data. *Inf. Sci.* **2017**, *409–410*, 68–86. [[CrossRef](#)]
186. Ji, C.; Ma, F.; Wang, J.; Sun, W. A Conditional Entropy Based Feature Selection for Soft Sensor Development in Chemical Processes. *Chem. Eng. Trans.* **2023**, *103*, 61–66. [[CrossRef](#)]
187. Vilsen, S.B.; Stroe, D.-I. Battery state-of-health modelling by multiple linear regression. *J. Clean. Prod.* **2021**, *290*, 125700. [[CrossRef](#)]
188. Nuhic, A.; Terzimehic, T.; Soczka-Guth, T.; Buchholz, M.; Dietmayer, K. Health diagnosis and remaining useful life prognostics of lithium-ion batteries using data-driven methods. *J. Power Sources* **2013**, *239*, 680–688. [[CrossRef](#)]
189. Meng, J.; Cai, L.; Luo, G.; Stroe, D.-I.; Teodorescu, R. Lithium-ion battery state of health estimation with short-term current pulse test and support vector machine. *Microelectron. Reliab.* **2018**, *88–90*, 1216–1220. [[CrossRef](#)]
190. Qin, T.; Zeng, S.; Guo, J. Robust prognostics for state of health estimation of lithium-ion batteries based on an improved PSO–SVR model. *Microelectron. Reliab.* **2015**, *55*, 1280–1284. [[CrossRef](#)]
191. Yang, D.; Zhang, X.; Pan, R.; Wang, Y.; Chen, Z. A novel Gaussian process regression model for state-of-health estimation of lithium-ion battery using charging curve. *J. Power Sources* **2018**, *384*, 387–395. [[CrossRef](#)]
192. Chen, T.; Morris, J.; Martin, E. Gaussian process regression for multivariate spectroscopic calibration. *Chemom. Intell. Lab. Syst.* **2007**, *87*, 59–71. [[CrossRef](#)]
193. Qu, J.; Liu, F.; Ma, Y.; Fan, J. A Neural-Network-Based Method for RUL Prediction and SOH Monitoring of Lithium-Ion Battery. *IEEE Access* **2019**, *7*, 87178–87191. [[CrossRef](#)]
194. He, J.; Tian, Y.; Wu, L. A hybrid data-driven method for rapid prediction of lithium-ion battery capacity. *Reliab. Eng. Syst. Saf.* **2022**, *226*, 108674. [[CrossRef](#)]
195. Fasahat, M.; Manthouri, M. State of charge estimation of lithium-ion batteries using hybrid autoencoder and Long Short Term Memory neural networks. *J. Power Sources* **2020**, *469*, 228375. [[CrossRef](#)]
196. Tang, A.; Huang, Y.; Liu, S.; Yu, Q.; Shen, W.; Xiong, R. A novel lithium-ion battery state of charge estimation method based on the fusion of neural network and equivalent circuit models. *Appl. Energy* **2023**, *348*, 121578. [[CrossRef](#)]
197. Nuroldayeva, G.; Serik, Y.; Adair, D.; Uzakbaiuly, B.; Bakenov, Z. State of Health Estimation Methods for Lithium-Ion Batteries. *Int. J. Energy Res.* **2023**, *2023*, 4297545. [[CrossRef](#)]

198. Shah, A.R.Y.; Shah, K.S.; Shah, C.R.; Shah, M.A. State of charge, remaining useful life and knee point estimation based on artificial intelligence and Machine learning in lithium-ion EV batteries: A comprehensive review. *Renew. Energy Focus* **2022**, *42*, 146–164. [[CrossRef](#)]
199. Hou, J.; Xu, J.; Lin, C.; Jiang, D.; Mei, X. State of charge estimation for lithium-ion batteries based on battery model and data-driven fusion method. *Energy* **2024**, *290*, 130056. [[CrossRef](#)]

**Disclaimer/Publisher’s Note:** The statements, opinions and data contained in all publications are solely those of the individual author(s) and contributor(s) and not of MDPI and/or the editor(s). MDPI and/or the editor(s) disclaim responsibility for any injury to people or property resulting from any ideas, methods, instructions or products referred to in the content.